

Experimental investigation on mechanical damage characteristics of sandstone under triaxial cyclic loading

Sheng-Qi Yang,^{1,2} P. G. Ranjith,² Yan-Hua Huang,¹ Peng-Fei Yin,¹ Hong-Wen Jing,¹ Yi-Lin Gui² and Qing-Lei Yu^{2,3}

¹State Key Laboratory for Geomechanics and Deep Underground Engineering, School of Mechanics and Civil Engineering, China University of Mining and Technology, Xuzhou 221116, China. E-mail: yangsqi@hotmail.com

²Deep Earth Energy Research Laboratory, Department of Civil Engineering, Monash University, Melbourne, VIC 3800, Australia

³School of Resource and Civil Engineering, Northeastern University, Shenyang, Liaoning 110819, China

Accepted 2015 January 13. Received 2015 January 13; in original form 2014 September 21

SUMMARY

The mechanical damage characteristics of sandstone subjected to cyclic loading is very significant to evaluate the stability and safety of deep excavation damage zones. However to date, there are very few triaxial experimental studies of sandstone under cyclic loading. Moreover, few X-ray micro-computed tomography (micro-CT) observations have been adopted to reveal the damage mechanism of sandstone under triaxial cyclic loading. Therefore, in this research, a series of triaxial cyclic loading tests and X-ray micro-CT observations were conducted to analyse the mechanical damage characteristics of sandstone with respect to different confining pressures. The results indicated that at lower confining pressures, the triaxial strength of sandstone specimens under cyclic loading is higher than that under monotonic loading; whereas at confining pressures above 20 MPa, the triaxial strength of sandstone under cyclic loading is approximately equal to that under monotonic loading. With the increase of cycle number, the crack damage threshold of sandstone first increases, and then significantly decreases and finally remains constant. Based on the damage evolution of irreversible deformation, it appears that the axial damage value of sandstone is all higher than the radial damage value before the peak strength; whereas the radial damage value is higher than the axial damage value after the peak strength. The evolution of Young's modulus and Poisson's ratio of sandstone can be characterized as having four stages: (i) *Stage I*: material strengthening; (ii) *Stage II*: material degradation; (iii) *Stage III*: material failure and (iv) *Stage IV*: structure slippage. X-ray micro-CT observations demonstrated that the CT scanning surface images of sandstone specimens are consistent with actual surface crack photographs. The analysis of the cross-sections of sandstone supports that the system of crack planes under triaxial cyclic loading is much more complicated than that under triaxial monotonic loading. More axial and lateral tensile cracks were observed in the specimens under cyclic loading than under monotonic loading.

Key words: Rock and mineral magnetism; Geomechanics; Fractures and faults; Asia.

1 INTRODUCTION

In all kinds of rock engineering, such as deep underground engineering, high slope engineering, dam base engineering and nuclear waste disposition projects, due to the influence of strong blasting and excavation disturbance, the rock mass often experiences cyclic loading, which leads to the continuous damage failure of tunnel (Zhu *et al.* 2010; Xu *et al.* 2012). Previous experimental studies have demonstrated that the mechanical behaviour of rocks under cyclic loading is significantly different from those under monotonic loading (Rao & Ramana 1992; Bagde & Petros 2005; Heap *et al.* 2009a,b; Ma *et al.* 2013; Wang *et al.* 2013). Therefore, it is very

important to investigate the mechanical damage characteristics of rock subjected to cyclic loading to better understand the unstable failure mechanism of rock engineering.

Uniaxial compression and tension testing are conventionally used to investigate the strength, deformation behaviour and failure characteristics of rock material subjected to cyclic loading. Using ultrasonic and acoustic emission (AE) monitoring techniques, Rao & Ramana (1992) investigated the progressive failure characteristics of granite under uniaxial cyclic loading. Akesson *et al.* (2004) investigated the crack initiation and propagation characteristics of an isotropic granite during uniaxial cyclic loading. Xiao *et al.* (2010) studied the fatigue damage characteristics of granite under uniaxial

cyclic loading, and obtained the relation between damage variable and cycle number. Erarslan & Williams (2012) presented the experimental results of strength and deformation behaviours of Brisbane tuff disk specimens under indirect cyclic tension. Their results showed that a macroscale splitting crack with a sharp and rough surface was found along the diametric compressive direction under monotonic loading, whereas an excessive amount of small particles and dust was produced under cyclic loading. Wang *et al.* (2013) examined the fatigue behaviour of granite under triaxial cyclic loading by performing a series of laboratory tests. The results showed that the axial residual strain decreased with cycle number when the peak deviatoric stress was less than the threshold for fatigue failure, whereas the axial residual strain increased with cycle number when the maximum stress was higher than the threshold. Liu *et al.* (2014) carried out uniaxial cyclic tests to investigate the damage evolution of rock salt. The results showed that the stress levels leading to the initiation and accelerated accumulation of fatigue damage under cyclic loading process were between 20 and 40 per cent of the uniaxial compressive strength (UCS) of the tested rock salt. In addition, shear testing is used to investigate the mechanical behaviour of rock under cyclic shear loading. In accordance with the shear test results of rock joints under cyclic loading, Jafari *et al.* (2003) found that the shear strength of joints depended on not only shearing velocity, but also the number of loading cycles and stress amplitude.

Sandstone, a type of sedimentary rock, is ubiquitous in underground engineering. In the past, the mechanical behaviour of sandstone under cyclic loading has been experimentally studied (Bieniawski 1971). Gatelier *et al.* (2002) carried out an extensive laboratory tests on the mechanical behaviour of an anisotropic porous sandstone under uniaxial and triaxial cyclic loading, which revealed two main mechanisms: compaction and microcracking. In the uniaxial tests, both mechanisms were shown to be strongly influenced by the inclination of loading with respect to the isotropy planes. However, with increased confining pressures, the influence of anisotropy was significantly reduced. On the basis of experimental results for intact sandstone under static and dynamic uniaxial cyclic loading, Bagde & Petros (2005) found that Young's modulus, UCS and stress energy increased with the loading frequency. Xu *et al.* (2009) carried out an experimental study on the damage process of sandstone by adopting the spatial AE technique. The experimental results showed that different damage types were located at different cyclic phases during the entire loading process. From initial damage in the static state phase to the early core region of cracks, the cracks expanded stably from the early core region at the beginning of the cycle and rapidly at the end of the cycle prior to the macroscopic failure of the rock. By conducting a series of laboratory tests, Liu & He (2012) and Liu *et al.* (2011) assessed the effects of frequency on the dynamic properties of sandstone specimens subjected to cycling loading under different confining pressures. Song *et al.* (2013) studied the damage evolution process and the crack development of sandstone using uniaxial cyclic testing and digital image correlation.

X-ray computed tomography (CT) is the best non-invasive non-destructive method to characterize complex pore structures, and has been applied to explore the internal damage behaviour of sandstone material under monotonic loading (Feng *et al.* 2004; Sufian & Russell 2013; Zhao *et al.* 2014). By adopting real-time X-ray CT, Feng *et al.* (2004) studied the damage evolution of sandstone under triaxial monotonic compression with chemical corrosion. They summarized that the CT value was the most important parameter describing the damage evolution process of rock. Using an X-ray CT system, Sufian & Russell (2013) investigated the microstructural pore changes and energy dissipation in Gosford sandstone during

pre-failure loading, but the stress condition was limited to uniaxial compression. Based on X-ray CT observations of Gosford sandstone under uniaxial compression, Zhao *et al.* (2014) analysed the mechanisms causing the strain rate dependency of the uniaxial tensile strength of Gosford sandstone using the distinct lattice spring model (DLSM). However, there are very few triaxial experimental studies of sandstone under cyclic loading. Moreover, few X-ray micro-CT observations have been adopted to reveal the damage mechanism of sandstone under triaxial cyclic loading. Therefore, in this paper, we report the results of a series of triaxial cyclic compression tests on sandstone under different confining pressures. Based on the experimental results, triaxial monotonic and cyclic mechanical parameters of sandstone specimens under different confining pressures are first compared. Then, the influence of cycle number on the crack damage threshold of sandstone is analysed. Next, using an X-ray micro-CT scanning system, the internal damage characteristics of sandstone material after triaxial monotonic and cyclic failure are explored. Finally, the influence of cycle number on the elastic modulus, Poisson's ratio and strain damage of sandstone under different confining pressures is discussed in detail.

2 TESTED ROCK MATERIAL AND TESTING METHOD

2.1 Sandstone material and testing equipment

The material used throughout this study was sandstone (a marine sedimentary rock) collected from the Shandong province in China. The sandstone is formed from cemented grains that may either be fragments of a pre-existing rock or monomineralic crystals. The cements binding these grains together are typically calcite, clays, and silica. According to the results of X-ray diffraction (XRD), the minerals in the sandstone material are feldspar, quartz, smectite, calcite and volcanic rock fragments (Fig. 1). A detailed composition of this rock is described as follows: the content (weight%) of feldspar is 50 per cent, quartz is 20 per cent, smectite is 15 per cent, calcite is 10 per cent and volcanic rock fragments is 5 per cent. The sandstone in this research is a fine- to medium-grained, feldspathic rock material with a connected porosity of 5.3 per cent and a bulk density of 2450 kg m^{-3} . All specimens were cored from the same block of material to an actual diameter of 49.3 mm and approximate 100 mm in length. All the experiments were performed on dry specimens at room temperature. The UCS of the sandstone was 83.14 MPa, and the elastic modulus (E_s) and Poisson's ratio (ν) of the sandstone under uniaxial compression were 13.95 GPa and 0.180, respectively. However, the peak axial strain (ϵ_{1c}) and peak radial strain (ϵ_{3c}) of the sandstone under uniaxial compression were 8.462×10^{-3} and -4.813×10^{-3} , respectively.

In the present research, a TAW-1000 servo-controlled rock mechanics experimental system was used to complete all experiments. The maximum loading capacity of the servo-controlled system is 1000 kN, and the maximum confining pressure is 60 MPa. During the experimentation, the axial force and the axial deformation were measured using an axial linear variable differential transducer (LVDT) with a range of 8 mm. The circumferential deformation was measured using an LVDT attached to a chain wrapped tightly around the specimen, for which the maximum displacement capacity was 4 mm. To eliminate the influence of end friction effects (Hawkes & Mellor 1970; Mogi 1996), the axial and circumferential LVDTs were located in the central part of the specimen.

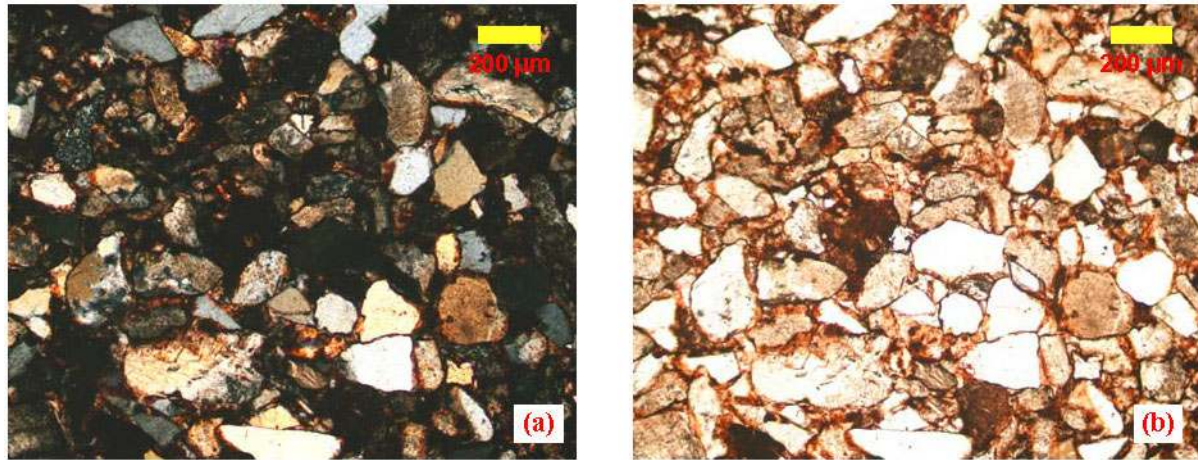


Figure 1. Thin section images of sandstone used in this research. (a) Crossed polarization photograph of microstructure. (b) Plane polarization photograph of microstructure.

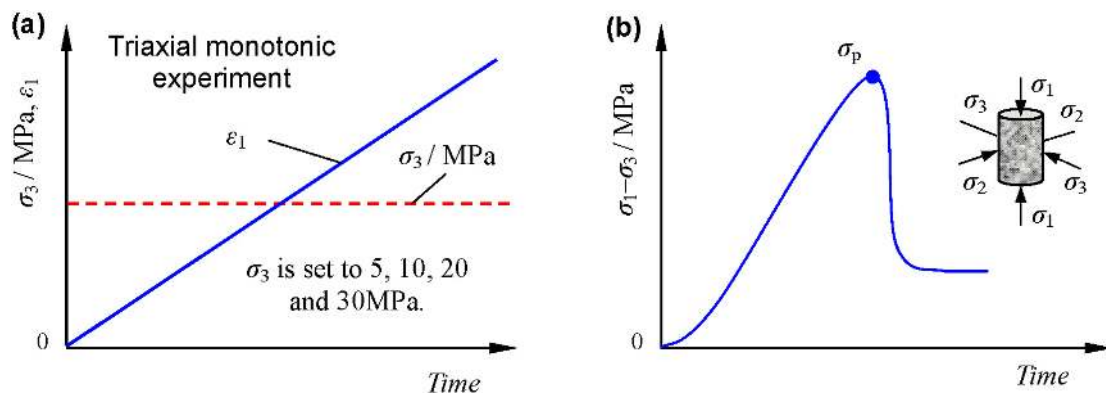


Figure 2. Monotonic loading path applied in the present research. (a) Variation of confining pressure and axial strain with time. (b) Variation of axial deviatoric stress with time.

2.2 Two types of triaxial tests

To investigate the evolution of the mechanical damage of the sandstone material, we performed two types of triaxial tests: (1) monotonic and (2) cyclic.

The triaxial monotonic experiments (Fig. 2; i.e. the conventional triaxial experiment) were carried out under different confining pressures (σ_3) of 5, 10, 20 and 30 MPa and consisted of the following two steps. First, the confining pressure was increased to the desired value at a constant rate of 0.5 MPa s^{-1} to ensure that the specimen was under uniform hydrostatic stresses. The deviatoric stress ($\sigma_1 - \sigma_3$) was then applied to the surface of the specimen at a constant axial displacement rate of 0.08 mm min^{-1} until failure. In Fig. 2, ε_1 means the axial strain.

The triaxial cyclic experiments (Fig. 3) were conducted using the following three steps. First, the hydrostatic pressure was applied to the specimen at a rate of 0.5 MPa s^{-1} until the desired value was reached. Second, the specimens were loaded to the first displacement value (corresponding to the first deviatoric stress level) at a controlled axial displacement rate of 0.08 mm min^{-1} , and then the first deviatoric stress level was unloaded to zero at a controlled axial force of 0.5 kN s^{-1} . In each subsequent cycle the second deviatoric stress level was increased and specimens again unloaded to zero. Finally, stress-cycling was continued in this way until specimens eventually failed. It should be noted that in our study, after the peak strength, two or three cyclic loading were still continued in order to analyse the mechanical behaviours of fractured rock material, which

is a different procedure to that used in previous studies (Heap *et al.* 2009b; Trippetta *et al.* 2013). Fig. 4 shows a typical experimental result of the triaxial cyclic loading path for a sandstone specimen that failed on the 15th loading cycle.

3 ANALYSIS OF TRIAXIAL CYCLIC EXPERIMENTAL RESULTS

3.1 Comparison between monotonic and cyclic experimental results

Fig. 5 shows typical triaxial cyclic experimental results of sandstone at $\sigma_3 = 5$ and 20 MPa. In Fig. 5, the triaxial monotonic experimental curves of sandstone are also given for comparison purposes. It should be noted that even after the peak stress, the specimens still continued to perform cyclic loading until the residual strength, which was usually difficult to carry out due to the sudden brittle failure of rock material after the peak strength.

Based on the triaxial experimental results of sandstone under monotonic and cyclic loading (Fig. 5), Fig. 6 presents the comparison of peak strength between monotonic and cyclic loading. From Fig. 6, we can see an obvious difference between monotonic and cyclic triaxial strength, and the difference changes with different confining pressures. Table 1 lists the comparison between monotonic and cyclic triaxial strength of sandstone. It should be noted that in Table 1, the monotonic triaxial strength of sandstone is the

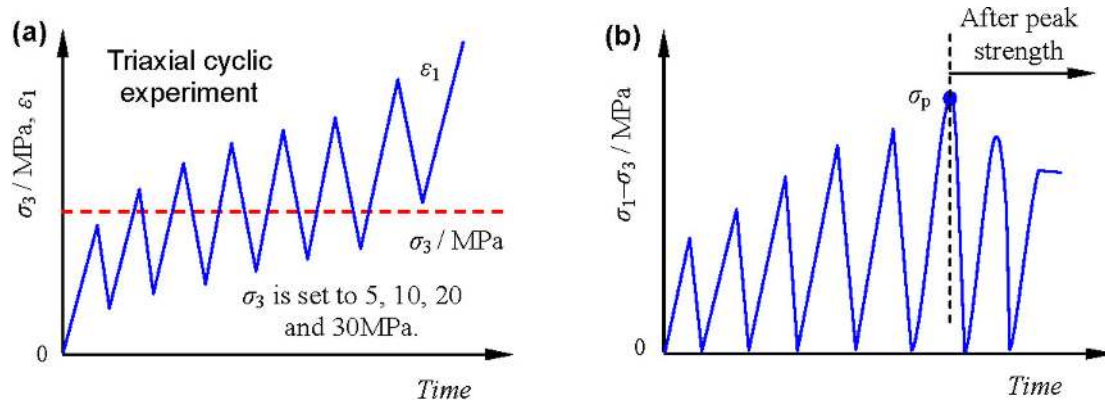


Figure 3. Cyclic loading path applied in the present research. (a) Variation of confining pressure and axial strain with time. (b) Variation of axial deviatoric stress with time.

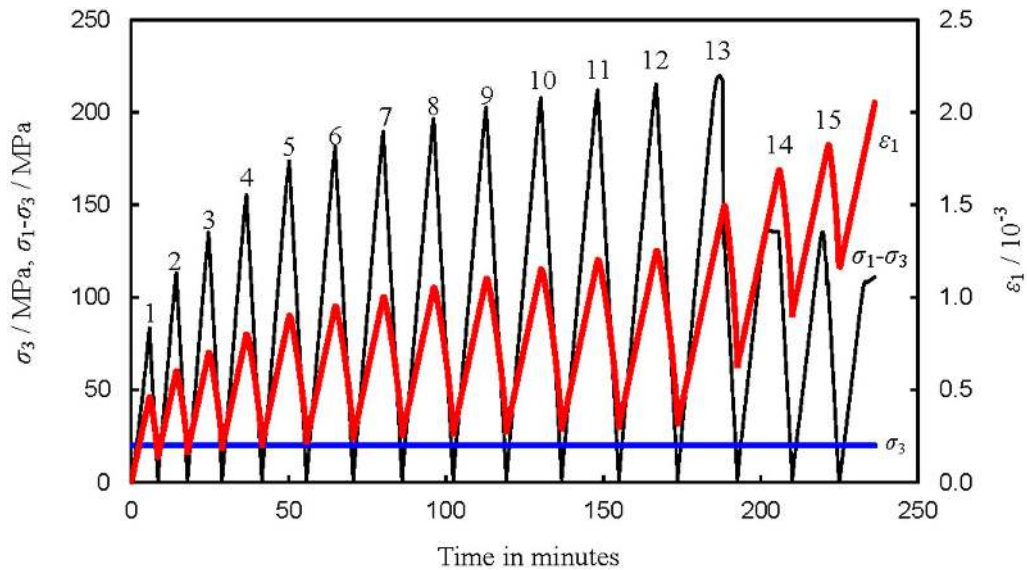


Figure 4. A typical experimental result of cyclic loading path from increasing amplitude, cyclic stressing triaxial experiment on sandstone specimen that failed during the 15th loading cycle. The numbers in this figure represent the cycle number. The red line represents the axial strain, the blue line represents the confining pressure and the black line represents the axial deviatoric stress.

average value of the tested specimens. From Table 1, it can be seen that $\sigma_3 = 5$ and 10 MPa, the cyclic triaxial strength of sandstone is higher than the monotonic triaxial strength. For $\sigma_3 = 5$ MPa, the difference between the cyclic and monotonic triaxial strength of sandstone is 12.75 MPa. As the confining pressure increases from 5 to 10 MPa, the difference between the cyclic and monotonic triaxial strength of sandstone decreases from 12.75 to 5.99 MPa. However, at $\sigma_3 = 20$ and 30 MPa, the cyclic triaxial strength of sandstone is approximately equal to the monotonic triaxial strength, which indicates that at higher confining pressure, cyclic loading does not affect the triaxial strength of sandstone compared with monotonic loading.

In order to analyse the difference of elastic modulus obtained by monotonic and cyclic loading testing, the deviatoric stress–axial strain of sandstone under cyclic unloading is compared with the monotonic loading curve of sandstone, and the results are shown in Fig. 7. Under cyclic loading condition, the elastic modulus of sandstone can be confirmed by the average slope at the stage of elastic deformation, and the dotted line shown in Fig. 7. Table 2 lists the comparison between the monotonic and cyclic triaxial elastic modulus of sandstone. From Table 2, it can be seen that at $\sigma_3 = 5$

10 MPa, the cyclic triaxial elastic modulus of sandstone is higher than the monotonic triaxial elastic modulus. For $\sigma_3 = 5$ MPa, the difference between the cyclic and monotonic triaxial elastic modulus of sandstone is 1.51 GPa. As the confining pressure increases from 5 to 10 MPa, the difference between the cyclic and monotonic triaxial elastic modulus of sandstone decreases from 1.51 to 0.60 GPa. However, at $\sigma_3 = 20$ and 30 MPa, the cyclic triaxial elastic modulus of sandstone is approximately equal to the monotonic triaxial elastic modulus, which indicates that at higher confining pressure, cyclic loading does not influence the triaxial elastic modulus of sandstone.

The influence of confining pressure on the difference between monotonic and cyclic triaxial strength and elastic modulus of sandstone results from the following reason. Under the lower confining pressures, with the increase of axial deformation, the rock specimen allows local yield to occur (Yang *et al.* 2011). Therefore, after local yield, extruded and fractured material in the rock can fill in the internal voids of specimens and strengthens the supporting structure in the rock material, as shown in Figs 7(a) and (b). Therefore, the cyclic triaxial strength and elastic modulus of sandstone are higher than the monotonic triaxial strength and elastic modulus at lower confining pressures. However, with the increase of confining

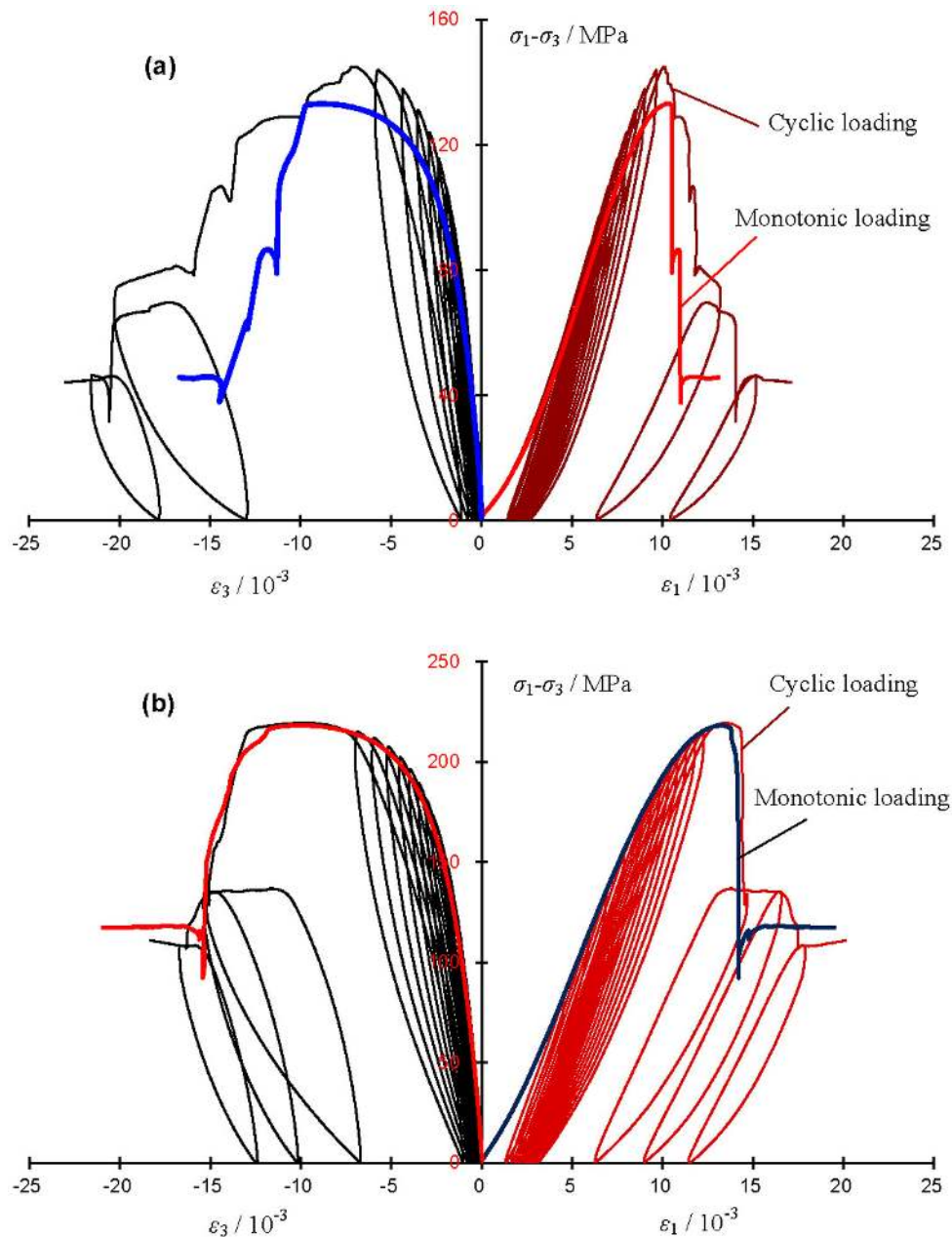


Figure 5. Comparison of monotonic and cyclic stress–strain curves of sandstone. (a) $\sigma_3 = 5$ MPa. (b) $\sigma_3 = 20$ MPa.

pressure, even though local yield still occurs with increasing deformation, extruded and fractured materials in the rock find it more and more difficult to fill in the internal voids due to the obvious decrease of porosity as the confining pressure increases. After the confining pressure is increased to 20 MPa, the porosity of sandstone will decrease less easily with increasing confining pressure and the supporting structure in the rock material cannot be strengthened any more (Figs 7c and d), which results in approximate equality between the cyclic and monotonic triaxial strength and elastic modulus.

3.2 Evolution of crack damage threshold

The crack damage threshold of rock specimens (Wong *et al.* 1997; Fairhurst & Hudson 1999; Heap *et al.* 2009a) can be confirmed

by the corresponding axial deviatoric stress where the volumetric deformation of the specimen switches from compaction-dominated to dilatancy-dominated (Yang *et al.* 2012; Yang & Jing 2013). Fig. 8 shows the typical evolution of the crack damage threshold of a sandstone specimen under triaxial cyclic loading.

In accordance with the relation between deviatoric stress–volumetric strains as shown in Fig. 8, the values of the crack damage threshold (σ_{cd}) of sandstone specimen under cyclic loading were confirmed, and the results are listed in Table 3. The σ_{cd} of sandstone specimen under monotonic loading is also listed in Table 3 to enable a comparison. Based on the data listed in Table 3, the relation between crack damage threshold of sandstone specimen and cycle number is shown in Fig. 9.

Fig. 9 indicates that when cycle number is less than 3, the sandstone specimen does not switch from compaction-dominated to

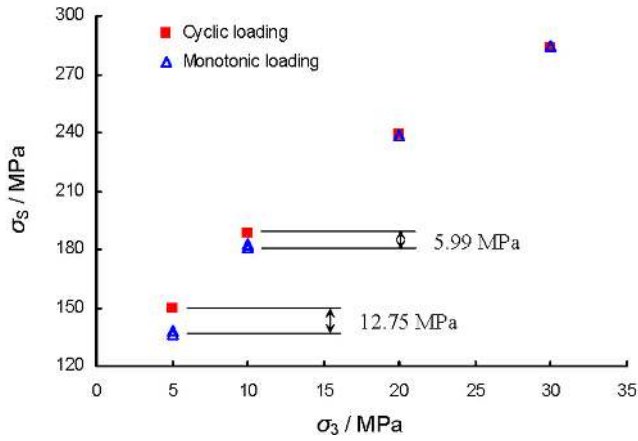


Figure 6. Comparison of monotonic and cyclic triaxial strength of sandstone specimen under different confining pressures. The denoted values mean the difference between monotonic and cyclic triaxial strength.

Table 1. Comparison of monotonic and cyclic triaxial strength (unit: MPa) of sandstone.

Loading path	$\sigma_3 = 5$ MPa	$\sigma_3 = 10$ MPa	$\sigma_3 = 20$ MPa	$\sigma_3 = 30$ MPa
Monotonic loading	137.24	181.97	238.30	284.25
Cyclic loading	149.99	187.96	239.55	283.31

dilatancy-dominated, that is the σ_{cd} of the specimen cannot be obtained. At the same confining pressure, the first σ_{cd} of the sandstone specimen under cyclic loading is approximately equal to that under monotonic loading, which indicates that the discreteness of the

Table 2. Comparison of monotonic and cyclic triaxial elastic modulus (unit: GPa) of sandstone.

Loading path	$\sigma_3 = 5$ MPa	$\sigma_3 = 10$ MPa	$\sigma_3 = 20$ MPa	$\sigma_3 = 30$ MPa
Monotonic loading	17.89	20.32	21.87	22.64
Cyclic loading	19.40	20.92	21.63	22.71

tested sandstone specimens is very small in the present research. With the increase of cycle number, the crack damage threshold of sandstone specimens first increases. For example at $\sigma_3 = 20$ MPa, the σ_{cd} value of sandstone increases from 131.14 to 154.58 MPa, because the closed cracks after unloading are more difficult to re-open with the increase of cycle number in the early cycles. Then, the σ_{cd} value decreases from 154.58 to 60.05 MPa, which can be explained as follows. On one hand, the closed cracks after unloading are easier to re-open with the increase of cycle number; on the other hand, some new cracks in the specimen are initiated, and propagate and coalesce with the increase of cycle number. Finally, when the specimen enters the stage of residual strength, the σ_{cd} value remains unaffected by cycle number.

Fig. 10 depicts the influence of confining pressure on the evolution of the crack damage threshold of sandstone. In general, the σ_{cd} value of sandstone specimen under higher confining pressure is greater than that under lower confining pressure. Moreover, the confining pressure does not affect the evolution characteristics of the crack damage threshold. Fig. 11 illustrates the relation between cycle number and the corresponding volumetric strain ($\epsilon_{cd,v}$) reaching the crack damage threshold of sandstone specimen under different

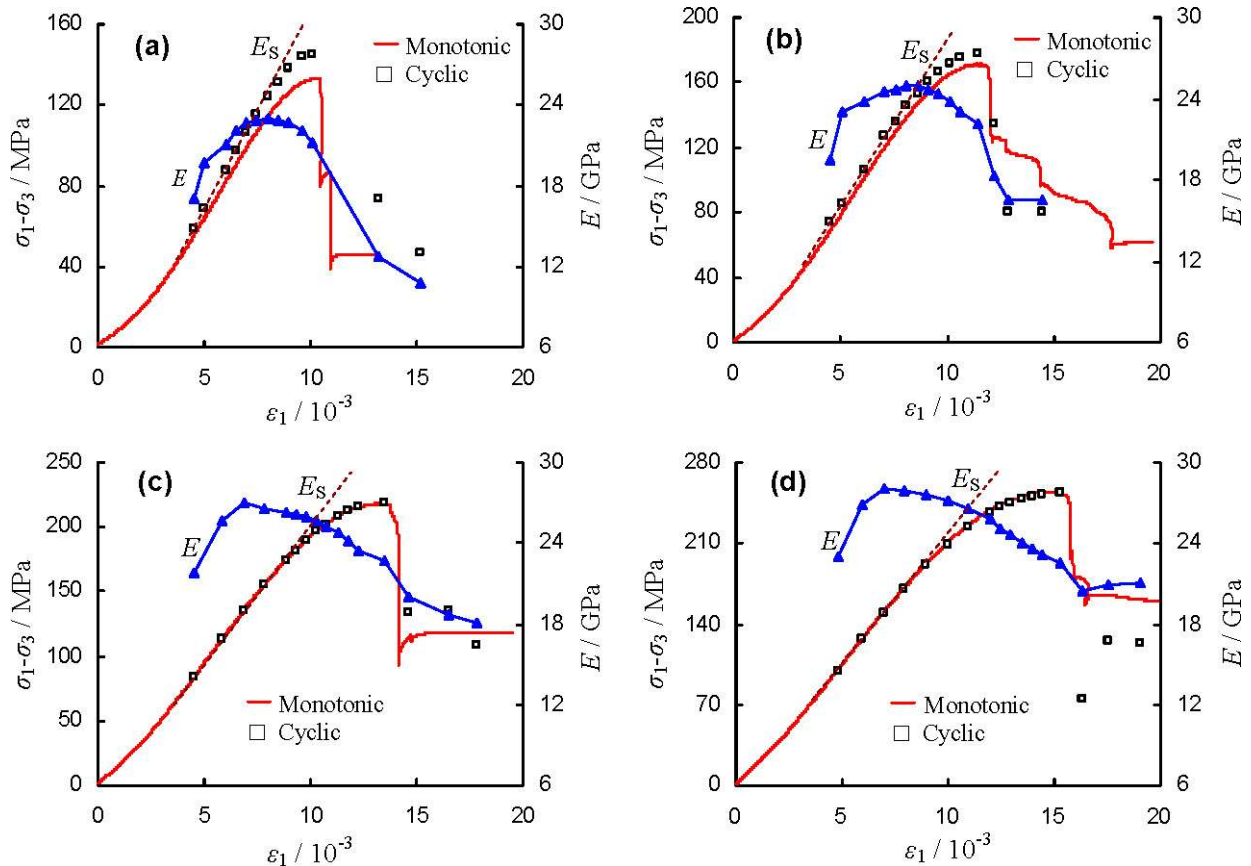


Figure 7. Comparison of monotonic and cyclic triaxial elastic modulus of sandstone specimen under different confining pressures. E represents Young's modulus and E_s represents the elastic modulus. (a) $\sigma_3 = 5$ MPa. (b) $\sigma_3 = 10$ MPa. (c) $\sigma_3 = 20$ MPa. (d) $\sigma_3 = 30$ MPa.

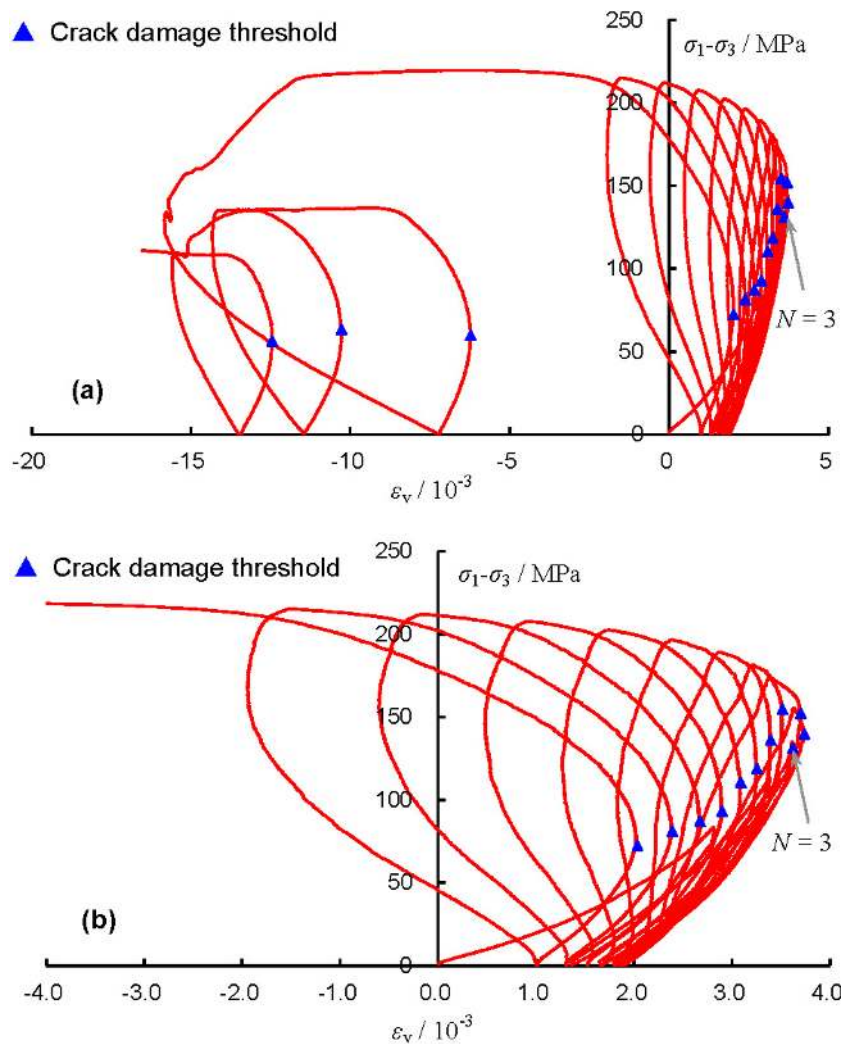


Figure 8. Typical evolution of crack damage threshold of sandstone specimen under triaxial cyclic loading ($\sigma_3 = 20$ MPa). (a) Relation between axial deviatoric stress and volumetric strain. (b) Local magnification.

Table 3. Values of crack damage threshold (σ_{cd}) of sandstone specimen under monotonic and cyclic loading (Unit: MPa).

Cycle number	$\sigma_3 = 5$ MPa	$\sigma_3 = 10$ MPa	$\sigma_3 = 20$ MPa	$\sigma_3 = 30$ MPa
Monotonic loading	74.88	102.50	138.35	167.11
3	78.98	98.47	131.14	—
4	87.17	105.29	139.79	163.78
5	86.62	114.34	151.93	174.81
6	85.64	98.76	154.58	179.40
7	75.79	89.23	136.15	171.48
8	64.17	81.25	118.77	140.64
9	55.01	64.84	110.44	126.10
10	42.53	61.54	92.95	117.55
11	36.36	54.23	86.99	111.76
12	27.95	49.51	81.23	106.38
13	22.03	38.35	72.42	99.29
14	—	38.52	60.05	94.05
15	—	45.44	63.42	68.12
16	—	—	56.28	72.02
17	—	—	—	66.24

Note: The crack damage threshold of sandstone specimen under monotonic loading is the average value.

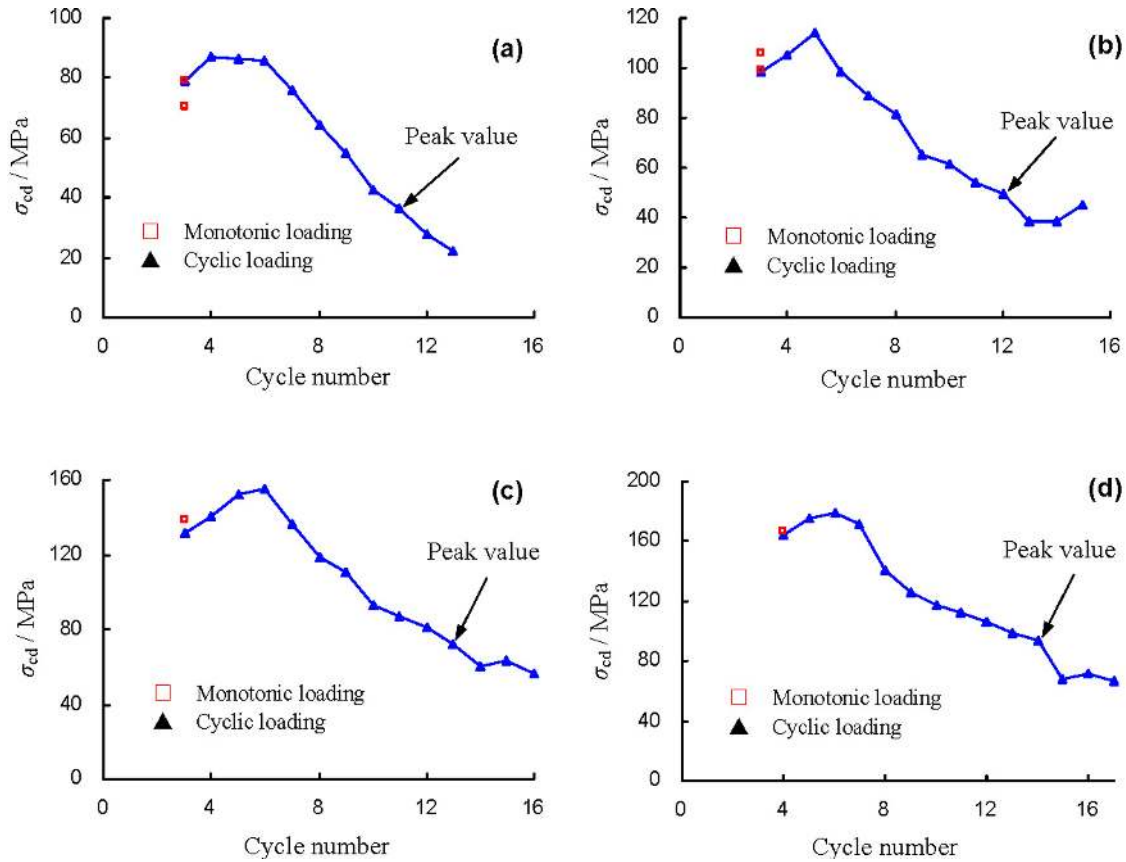


Figure 9. Relationship between crack damage threshold of sandstone specimen and cycle number. (a) $\sigma_3 = 5$ MPa. (b) $\sigma_3 = 10$ MPa. (c) $\sigma_3 = 20$ MPa. (d) $\sigma_3 = 30$ MPa.

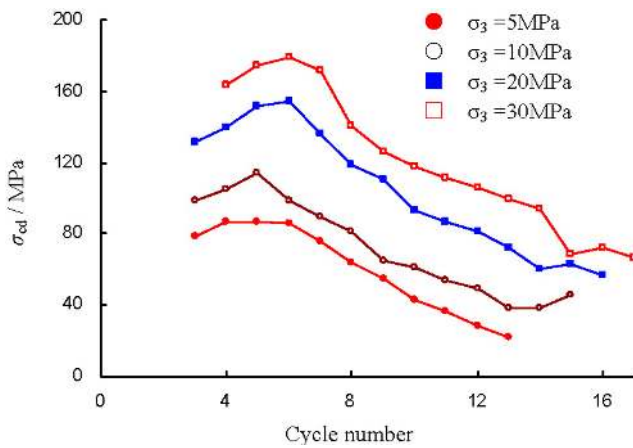


Figure 10. Influence of confining pressure on the evolution of crack damage threshold of sandstone specimen.

confining pressures. Fig. 11 shows that in the early cycles, the confining pressure has no great influence on the relation between $\varepsilon_{cd,v}$ and cycle number; whereas in later cycles, the confining pressure has a significant effect on the relation between $\varepsilon_{cd,v}$ and cycle number, especially after the peak strength. At the same cycle number, if the confining pressure is higher, the volumetric strain reaching the crack damage threshold will be lower due to the limitation of high confining pressure.

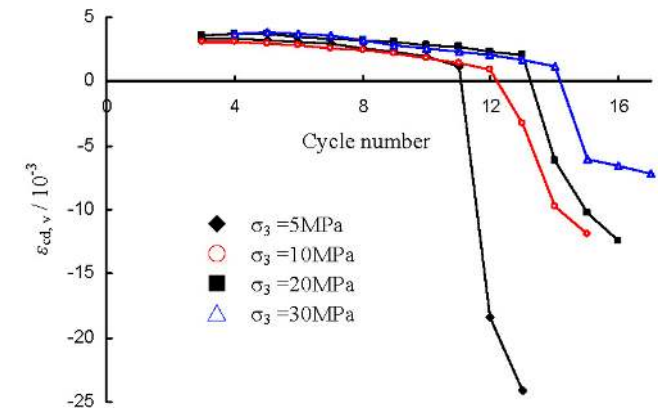


Figure 11. Relation between cycle number and the corresponding volumetric strain reaching crack damage threshold of sandstone specimen under different confining pressures.

4 MECHANISM OF MECHANICAL DAMAGE

4.1 X-ray micro-CT equipment and scanning procedure

X-ray CT scanning of the sandstone specimen was carried out using a Nanotom 160 high-resolution micro-CT at a spatial resolution of 30 μm . The X-ray beam penetrating the specimen is measured by an array of detectors. The X-ray is produced by electrons striking a Mo-W alloy target in an X-ray tube. The electron current was

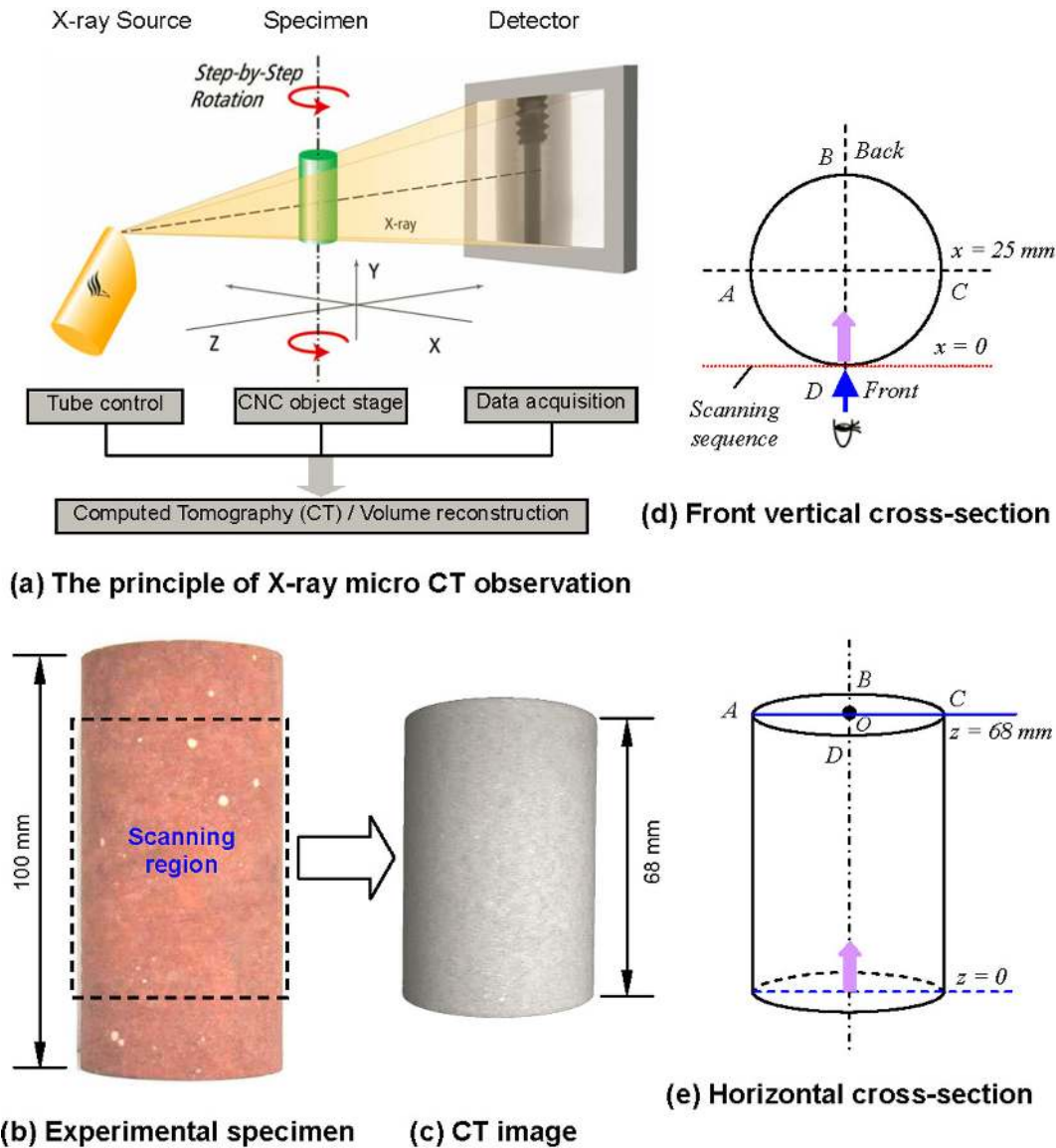


Figure 12. The principle of X-ray micro-CT observations and illustrations of the directions in which X-ray CT scanning was carried out and scanned cross-sections.

80 μA , the accelerating voltage was 140 kV, and the scanning time was 4 s. The degree of X-ray attenuation depends on the density and the atomic number of the materials in the specimens. Material with higher density and higher atomic number generally causes higher attenuation of the X-rays. X-ray projection data from various directions are obtained by the 360° rotation of the X-ray source (Fig. 12a). We collected a 2-D image at intervals of 0.18° , and thus 2000 slice images could be obtained for one specimen. A 2-D image representing the linear distribution of X-ray attenuation was reconstructed using Fourier transformation of the projection data. A 3-D data set of the specimen was obtained by stacking consecutive 2-D images.

It should be noted that only a cylinder 50 mm diameter and 68 mm length can be regarded as the scanning region, as shown in Figs 12(b) and (c). For the front vertical cross-section shown in Fig. 12(d), the slice images were captured at 0.5 mm intervals and the scanning sequence was from front to back. For the horizontal cross-section shown in Fig. 12(e), the slice images were captured at 0.03 mm

intervals, and each image was 0.03 mm thick. Therefore, a total of 2266 slice images were obtained in the X-ray micro-CT testing of each sandstone specimen. These slice images can be used to explore the internal damage of sandstone material under monotonic and cyclic loading.

4.2 Internal damage of sandstone under triaxial monotonic and cyclic loading

Figs 13 and 14 depict the comparison of X-ray micro-CT scanning surface images and actual surface crack photographs of sandstone specimen after triaxial monotonic and cyclic loading ($\sigma_3 = 5\text{ MPa}$), respectively. In Figs 13 and 14, black regions with lower CT numbers mean cracks, and other regions with higher CT numbers indicate no surface failure. From Figs 13 and 14, it can be seen that X-ray CT scanning surface images approximate the actual surface crack images, which demonstrates that X-ray micro-CT scanning can be well used to explore internal damage in sandstone material.

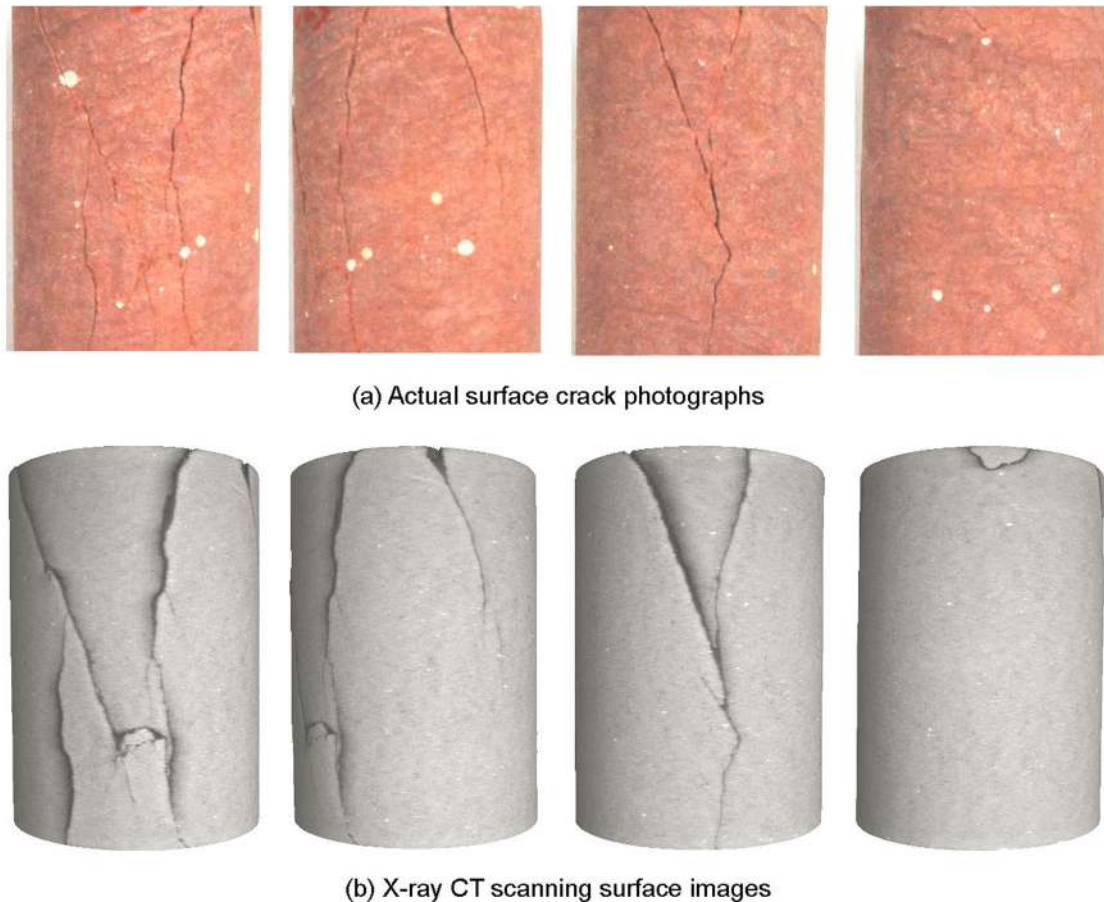


Figure 13. Comparison of X-ray CT scanning surface images and actual surface crack photographs of sandstone specimen after triaxial monotonic loading ($\sigma_3 = 5$ MPa). (a) Actual surface crack photographs. (b) X-ray CT scanning surface images.

Figs 15 and 16, respectively show horizontal cross-sections with different heights and front vertical cross-sections with different depths of sandstone specimen after triaxial monotonic failure ($\sigma_3 = 5$ MPa). From Fig. 15, we can analyse the effect of height (z) on the extent of internal damage to sandstone after triaxial monotonic failure. At $z = 5\text{--}15$ mm, the horizontal cross-section is located in the bottom region of the specimen, only one main crack across the diameter direction is observed and the system of cracks is very simple, which can also be demonstrated in the bottom region shown in Fig. 13. At $z = 15\text{--}45$ mm, the horizontal cross-section is located in the middle region of the specimen. Two bigger cracks are observed, resulting from the crack propagation and coalescence inside the specimen with the increase of deformation. The left crack in the specimen does not almost take place moving, whereas the right crack in the specimen moves gradually towards the right boundary at an angle of about 30° with the horizontal direction. However, at $z = 45\text{--}60$ mm, when the horizontal cross-section is located in the top region of the specimen, even though no new cracks are observed, the width of the two cracks begins to increase compared with those at $z = 15\text{--}45$ mm. Fig. 16 depicts the effect of depth (x) on the extent of internal damage to the sandstone material after triaxial monotonic loading. From Fig. 16, it is clear that two large cracks with ‘Y’ type are observed and the system of cracks is very simple.

For the two large cracks shown in Figs 13, 15 and 16, it is very difficult to distinguish which crack is shear failure or axial splitting tensile failure, only in accordance with the angle of the 2-D crack with the direction of major principal stress. For example, in Fig. 16, from CT images at $x = 5, 25$ and 45 mm, we can draw contradictory

conclusions on shear or tensile fracture. Therefore, we reconstructed 3-D images of the sandstone specimens before and after triaxial monotonic failure ($\sigma_3 = 5$ MPa). In the 3-D images, fracture regions with lower CT numbers are black, and other regions with relatively higher CT numbers are transparent, as shown in Fig. 17. From Fig. 17, we are able to confirm that 3-D crack 1 is axial splitting tensile fracture, and 3-D crack 2 is shear fracture.

Figs 18 and 19, respectively, show horizontal cross-sections with different heights and front vertical cross-sections with different depths for sandstone specimens after triaxial cyclic loading ($\sigma_3 = 5$ MPa). In general, in accordance with Figs 18 and 19, it can be seen that under triaxial cyclic loading, the system of cracks is more complicated than that under triaxial monotonic loading for the same confining pressure (Figs 15 and 16), which is also demonstrated from the comparison of surface cracks shown in Figs 13 and 14, respectively. Under triaxial cyclic loading, the specimen takes on a typical single shear fracture, and at the same time, axial and lateral tensile cracks are also observed, whereas under triaxial monotonic loading, no lateral cracks are observed. These shear fracture, axial and lateral tensile cracks under triaxial cyclic loading can be all further inferred from microscopic observations on the fracture surface of the failed specimen shown in Fig. 20.

In order to make a quantitative evaluation of the fracture extent of internal damage of sandstone specimen after triaxial monotonic and cyclic compression failure, each horizontal CT image shown in Figs 15 and 18 was processed using Matlab software (Gui, *et al.* 2012) and changed to binarized images (Fig. 21). In Fig. 21, the white regions represent the cracks, whereas the black regions

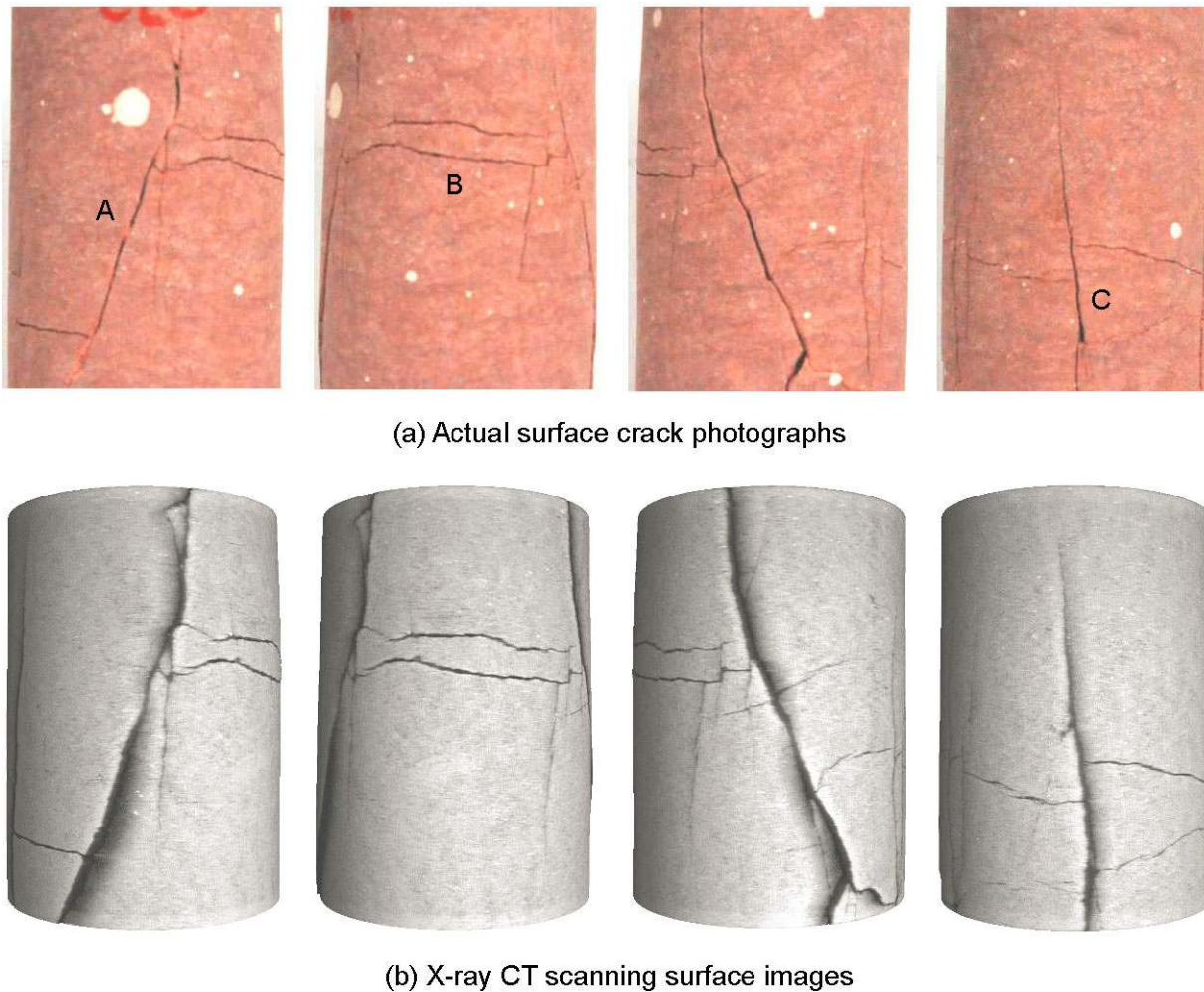


Figure 14. Comparison of X-ray CT scanning surface images and actual surface crack photographs of sandstone specimens after triaxial cyclic loading ($\sigma_3 = 5$ MPa). (a) Actual surface crack photographs. (b) X-ray CT scanning surface images.

represent intact rocks without any failure. Generally, the crack system in Fig. 21 approximates to the experimental results in Figs 15 and 18. On the basis of binarized images of all horizontal cross-sections of sandstone specimens after triaxial monotonic and cyclic compression failure, we obtained the crack area and aperture extent (i.e. the percentage ratio of crack area to entire area) for each horizontal cross-section. As a result, we were able to investigate quantitatively the effect of height (z) on the extent of internal damage of sandstone material after triaxial monotonic and cyclic compression failure.

Fig. 22 shows the evolution of crack area and aperture extent along different heights (z) of sandstone specimen after triaxial monotonic and cyclic compression failure. From Fig. 22(a), it can be seen that after triaxial monotonic compression failure, the crack area of sandstone specimens increases from 12.50 mm² at $z = 5$ mm to 27.80 mm² at $z = 65$ mm. In contrast, after triaxial cyclic compression failure, the crack area of sandstone specimens varies in a smaller range from 34.51 mm² at $z = 5$ mm to 39.01 mm² at $z = 40$ mm, and then decreases rapidly from 39.01 mm² at $z = 40$ mm to 7.21 mm² at $z = 65$ mm. From Fig. 22(b), we can see that the evolution of aperture extent approximates to that of the crack area. With the increase of height, the aperture extent of sandstone specimens after triaxial monotonic compression failure increases from 0.47 per cent at $z = 5$ mm to 1.05 per cent at $z = 65$ mm. However, after

triaxial cyclic compression failure, the aperture extent of sandstone specimens varies in a smaller range from 1.29 per cent at $z = 5$ mm to 1.46 per cent at $z = 40$ mm, and then decreases rapidly from 1.46 per cent at $z = 40$ mm to 0.27 per cent at $z = 65$ mm. Furthermore, at $z = 5$ –40 mm, the crack area and aperture extent of sandstone after cyclic failure are higher than those after monotonic failure. At $z = 40$ –50 mm, the crack area and aperture extent of sandstone after cyclic failure approximate to those after monotonic failure. However, at $z = 50$ –65 mm, the crack area and aperture extent of sandstone after cyclic failure are lower than those after monotonic failure.

5 DISCUSSION ON EVOLUTION OF DEFORMATION DAMAGE

In the past, many investigations have been conducted on the effect of cyclic loading on the elastic modulus and Poisson's ratio of rock material. However, and it has been found that the effect is dependent not only on the confining pressure but also on the softness and hardness. By carrying out uniaxial cyclic tests for hard basalt and granite, Heap *et al.* (2009b), and Heap & Faulkner (2008) demonstrated that cyclic stressing changes significantly the deformation parameters of basalt and granite. The Young's modulus decreases but the Poisson's ratio increases with the increase of cycle number.

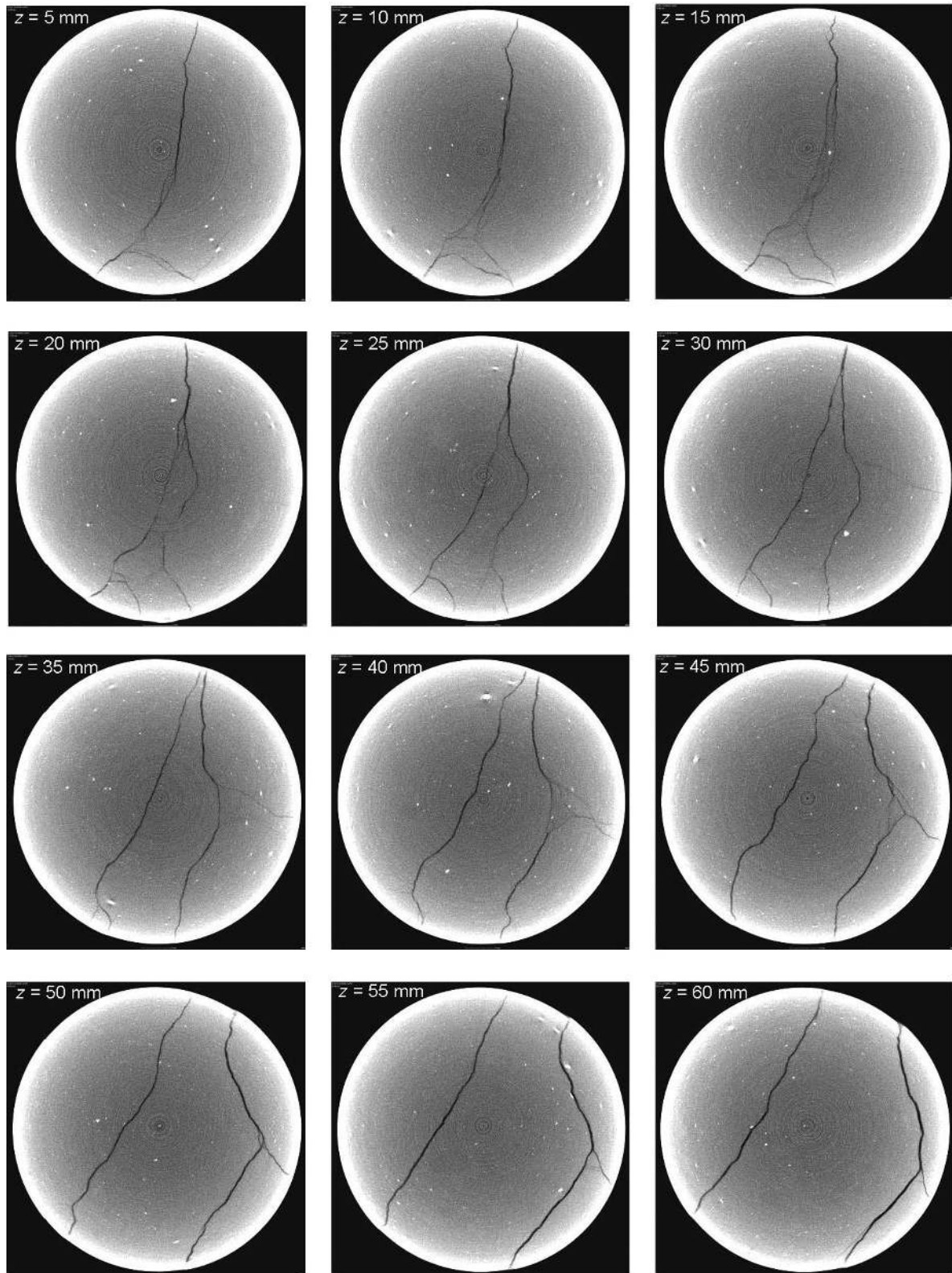


Figure 15. Horizontal cross-sections with different heights of sandstone specimens after triaxial monotonic loading ($\sigma_3 = 5$ MPa).

Moreover the variance of basalt in both E and ν did not depend on the action of high temperature treatment (Heap *et al.* 2009b). Fuenkajorn & Phueakphum (2010) performed a series of uniaxial cyclic tests on salt. They found that the elastic modulus of salt decreased slightly during the first few cycles, and tended to remain

constant until failure. Trippetta *et al.* (2013) reported laboratory measurements of Young's modulus and Poisson's ratio of soft gypsum and hard dolostones under uniaxial cyclic loading. A complex variation in E and ν was found as follows. In the early cycles, large increases in E and ν were observed, followed by essentially constant

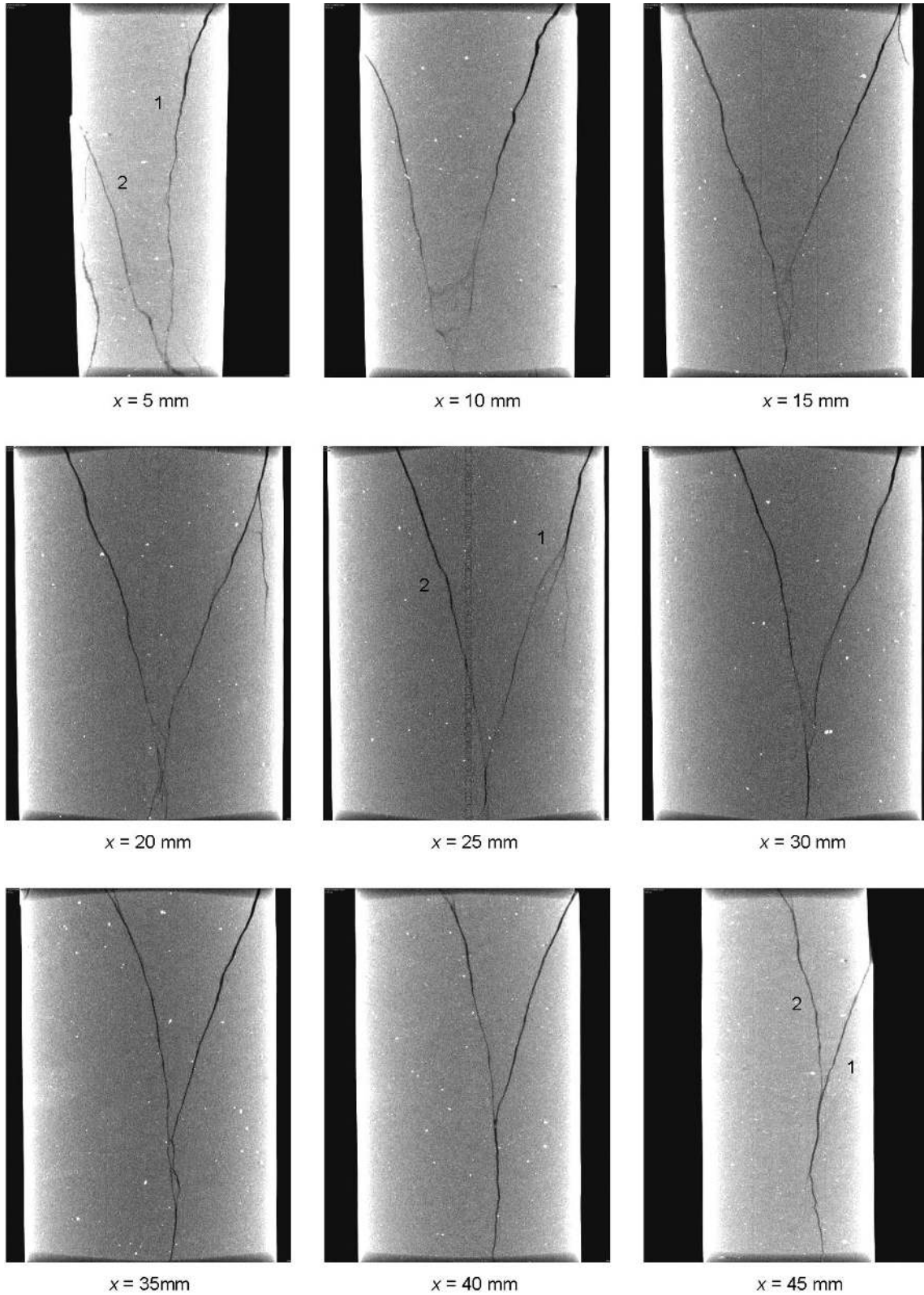


Figure 16. Front vertical cross-sections with different depths of sandstone specimens after triaxial monotonic loading ($\sigma_3 = 5$ MPa).

values, before E decreased and ν increased approaching failure. The above analysis shows that under uniaxial compression, the elastic modulus and Poisson's ratio of rocks with different softness and hardness have various evolution characteristics.

It should be noted that our research on sandstone specimen under triaxial cyclic loading differs from that reported in previous studies (Heap & Faulkner 2008; Heap *et al.* 2009b; Trippetta *et al.* 2013). Fig. 23 presents the evolution of elastic modulus and Poisson's ratio

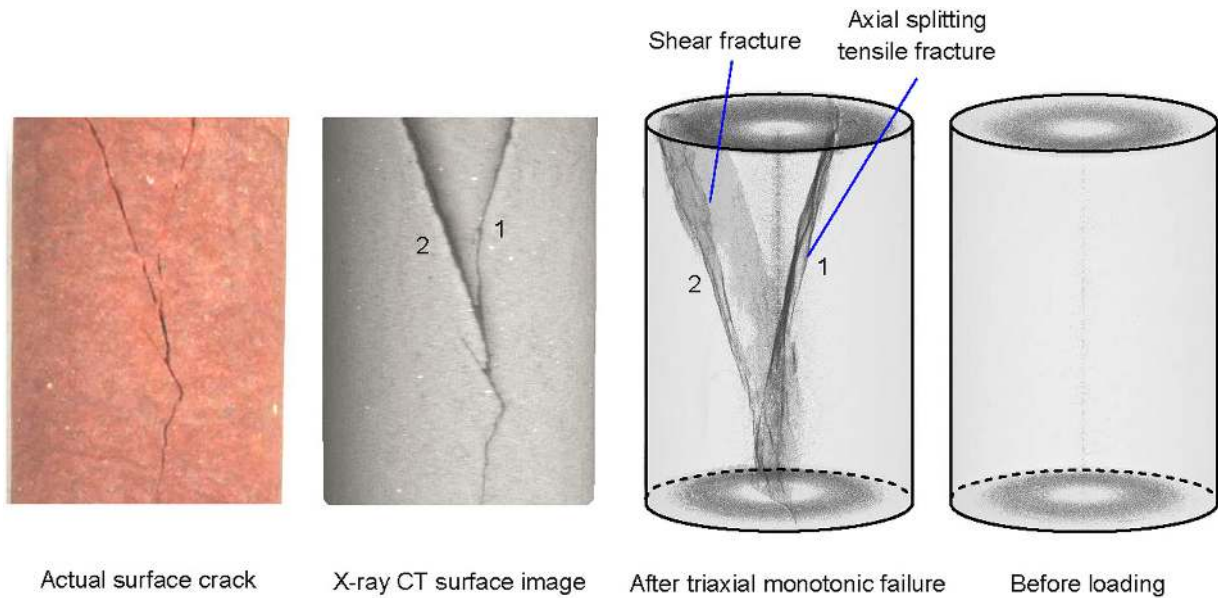


Figure 17. 3-D images of sandstone specimens before and after triaxial monotonic failure ($\sigma_3 = 5$ MPa). The numbers in the figure correspond to those shown in Fig. 16.

with increasing cycle number for sandstone specimens (derived from Fig. 5). The relationship between elastic modulus and axial strain of sandstone specimen for each cycle is also presented in Fig. 7 to demonstrate the influence of stress level on the evolution of elastic modulus. In accordance with Figs 7 and 23, the evolution can be characterized as having four stages (Fig. 24): (i) *Stage I*: material strengthening; (ii) *Stage II*: material degradation; (iii) *Stage III*: material failure and (iv) *Stage IV*: structure slippage.

During Stage I, the elastic modulus (E) increases obviously, whereas the Poisson's ratio (ν) first decreases and then increases slightly. The increase in E indicates that the specimens become stiffer and more difficult to deform. In previous studies of rocks under uniaxial cyclic loading (Heap *et al.* 2009b; Trippetta *et al.* 2013), the increase in elastic modulus usually contributes to the closure of pre-existing pores and fissures in the rock material. However, it should be noted that in our research, the unloading stress level of the sandstone specimen for the first cycle is located at the stage of elastic deformation in the monotonic loading curve (Fig. 7). Therefore, the closure of pre-existing pores and fissures cannot indicate clearly the evolution characteristics of the E and ν of sandstone material. New insights on the evolution can be presented as follows. On one hand, with the increase of cycling stress, some mesoscopic elements with lower strength and stiffness reach first their maximum supporting capacity, yield softening, and produce plastic deformation during the yielding of specimens (Yang *et al.* 2008). Some extruded and fractured elements can then fill in the internal voids of sandstone specimens. On the other hand, some pre-existing pores and fissures can also cause the closure (see Figs 24a and b). The above two factors strengthen the supporting structure of sandstone material, which results in the increase of E and the decrease of ν . Afterwards, with further increase of cycling stress, the rate of increase of elastic modulus becomes slower, and the Poisson's ratio begins to increase, which indicates that each increment of axial strain results in a larger increment of radial strain.

During Stage II, we observe a significant increase in ν , but a decrease in E , which is different from previously reported results of cyclic stressing experiments on softer rocks (Trippetta *et al.* 2013). However, our results are in good agreement with those on hard

rocks including sandstone, basalt and granite (Heap & Faulkner 2008; Heap *et al.* 2009b, 2010). At $\sigma_3 = 5$ MPa, the elastic modulus decreased slightly from 22.92 to 21.25 GPa, but the Poisson's ratio increased significantly from 0.237 to 0.462 during increasing amplitude cycling stressing to failure. However, at $\sigma_3 = 20$ MPa, the elastic modulus decreased greatly from 27.01 to 22.73 GPa, and the Poisson's ratio also increased obviously from 0.154 to 0.401. The decrease in E can be attributed to a progressive degradation in the stiffness of the rock due to the increase of crack damage with increasing cycle number. At higher stress level, each cycle applied to the specimen will produce an additional increment of crack damage, resulting in an increasing amount of irreversible deformation. The increase of ν during material degradation can be explained as follows. Due to the higher deviatoric stress level, in early cycles, some new cracks are initiated, propagated and coalesced (see Figs 24c and d). When the deviatoric stress is re-applied in subsequent loading cycles, these cracks can be re-opened more easily, which results in a high radial strain and a high Poisson's ratio.

During Stage III, it is very clear that the elastic modulus of sandstone specimen decreases and the Poisson's ratio increases. At $\sigma_3 = 5$ MPa, the elastic modulus decreases significantly from 21.25 to 12.71 GPa, but the Poisson's ratio increases sharply from 0.462 to 1.455 during this stage. However, at $\sigma_3 = 20$ MPa, the elastic modulus decreases from 22.73 to 18.69 GPa, and the Poisson's ratio also increases obviously from 0.401 to 0.904. The variance of E and ν of the sandstone specimen during this stage can be explained as follows. It should be noted that Stage III is entered after the peak strength, as shown in Fig. 8. Larger macroscopic cracks have formed at this stage, which results in the failure of the structure of the rock material (Fig. 24e). Therefore, the increase in the number of macroscopic cracks reduces the axial stiffness and simultaneously allows higher radial strain for the same level of applied deviatoric stress.

During Stage IV, the elastic modulus decreases slightly from 12.71 to 10.81 GPa, but the Poisson's ratio varies only slightly from 1.455 to 1.443 at $\sigma_3 = 5$ MPa. In contrast, at $\sigma_3 = 20$ MPa, the elastic modulus changes from 18.69 to 18.09 GPa, and the Poisson's ratio varies from 0.904 to 0.927. This indicates that neither the elastic

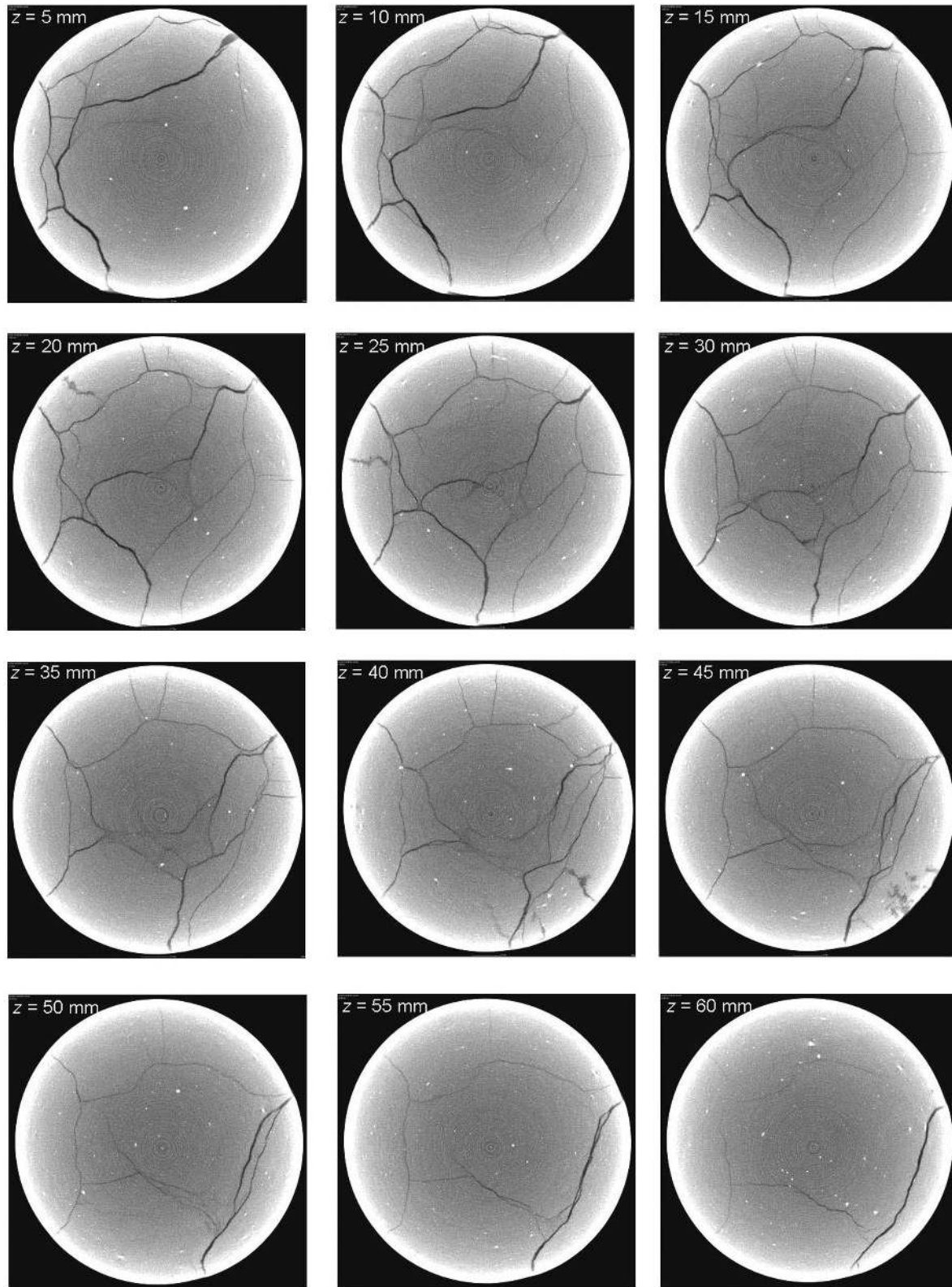


Figure 18. Horizontal cross-sections with different heights of sandstone specimens after triaxial cyclic loading ($\sigma_3 = 5$ MPa).

modulus nor the Poisson's ratio of sandstone are dependent on cycle number during this stage, for the following reason. Due to the constriction of confining pressure, the specimen has entered the stage of residual strength, and mainly supports the axial capacity by the friction slippage in the macroscopic failure plane (see Fig. 24f),

which results in no obvious variance in both the E and ν of sandstone specimens.

It should be noted that for the same cycle number, the elastic modulus of sandstone specimen before peak strength increases non-linearly with the increase of confining pressure (Yang *et al.* 2012;

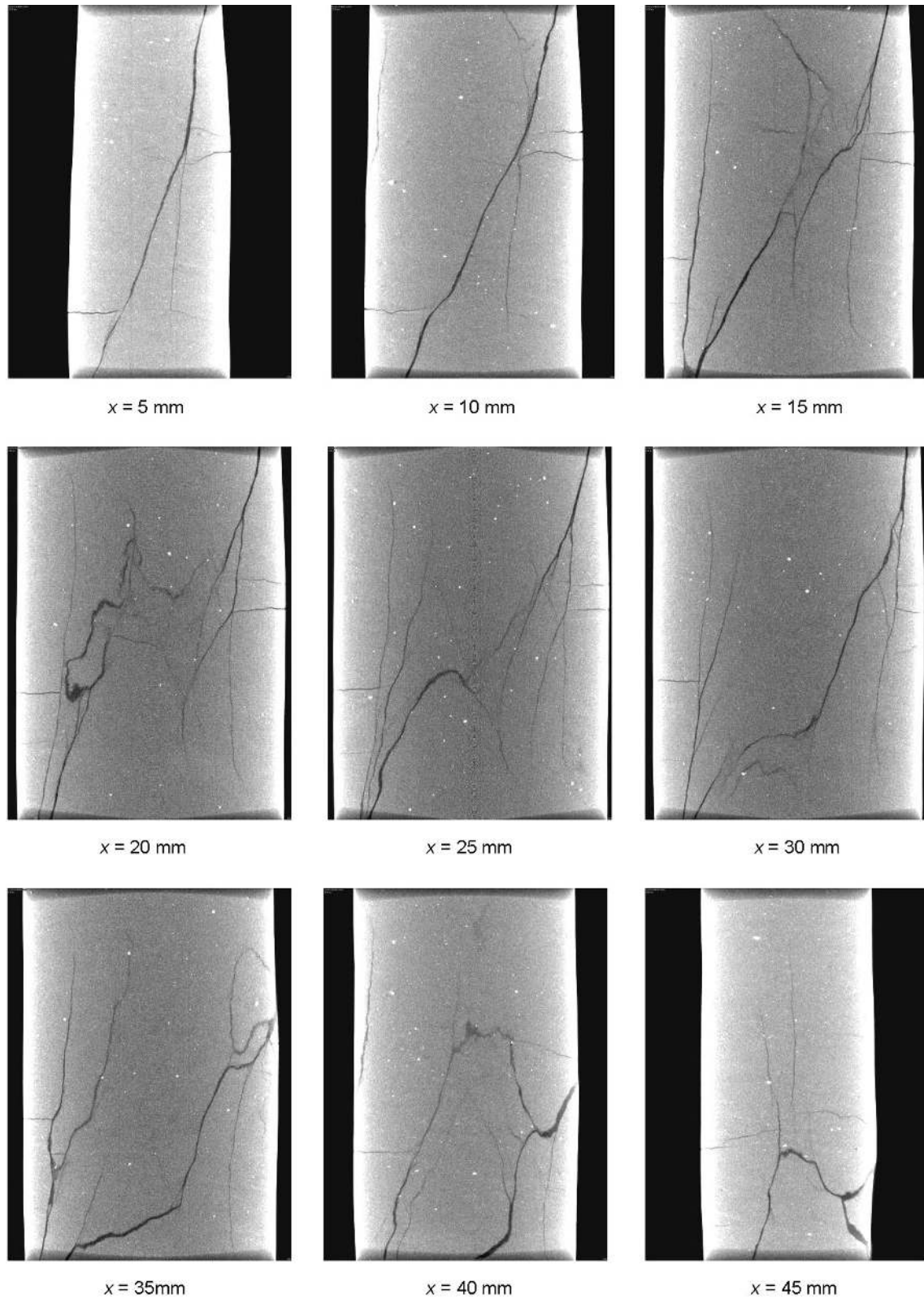


Figure 19. Front vertical cross-sections with different depths of sandstone specimens after triaxial cyclic loading ($\sigma_3 = 5$ MPa).

Yang & Jing 2013), whereas at higher confining pressures of 20 and 30 MPa, the elastic modulus is unaffected by confining pressure. In contrast, after the peak strength, with the increase of cycle number, the elastic modulus of sandstone specimen decreases more slowly for higher confining pressures, which indicates that the confining

pressure can also increase the axial stiffness of fractured rock material. However, in early cycles, the confining pressure has almost no effect on the relation between the Poisson's ratio of sandstone specimen and cycle number; but in later cycles, the Poisson's ratio of sandstone specimens is significantly dependent on the confining

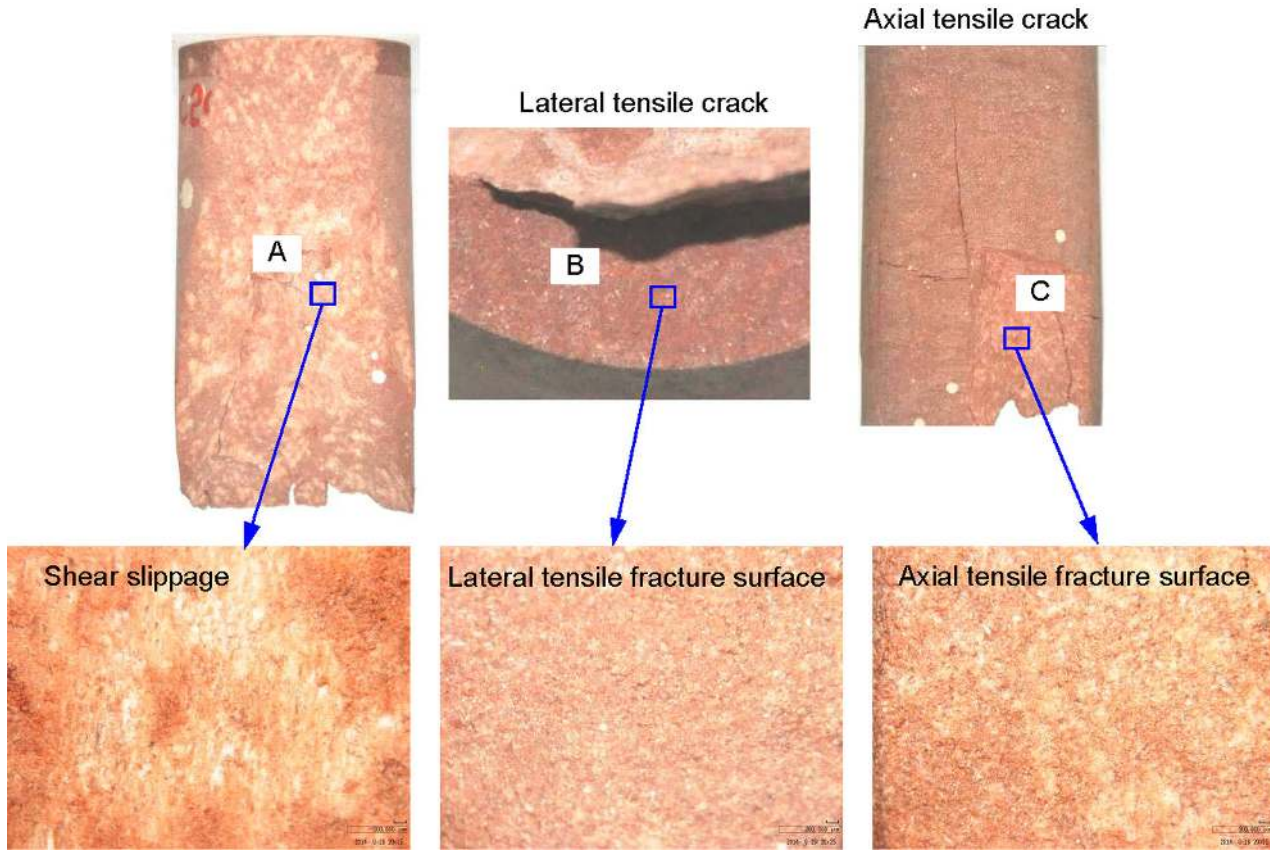


Figure 20. Microscopic observations on the fracture surface of sandstone specimens under triaxial cyclic loading ($\sigma_3 = 5$ MPa). The letters in this figure are corresponding to those shown in Fig. 14(a). Shear slippage indicates the shear crack, and tensile fracture surface means the tensile crack.

pressure. The Poisson's ratio of sandstone specimen under higher confining pressures is lower than that under lower confining pressures, which results from lower radial strains due to the constriction of higher confining pressures.

In order to quantitatively evaluate the damage extent of sandstone specimen under triaxial cyclic loading, the axial and radial damage variable are defined in accordance with the irreversible deformation (plastic deformation) for each cycle, which are expressed in eqs (1) and (2), respectively.

$$D_{\text{axial}} = \frac{(\varepsilon_1^p)_N}{\sum_{N=1}^m (\varepsilon_1^p)_N} \quad (1)$$

$$D_{\text{radial}} = \frac{(\varepsilon_3^p)_N}{\sum_{N=1}^m (\varepsilon_3^p)_N}, \quad (2)$$

where D_{axial} and D_{radial} represent the axial and radial damage variable of rock, respectively. ε_1^p and ε_3^p , means the irreversible deformation of rock and N indicates cycle number. The letter m represents the maximum cycle number.

Using eqs (1) and (2), the axial and radial damage value of sandstone specimen for each loading-unloading cycle can be confirmed in accordance with the deviatoric stress-strain curves shown in Fig. 5. Fig. 25 depicts the comparison between the axial and radial damage evolution of sandstone specimen under confining pressure. From Fig. 25, it can be seen that at the same confining pressure, the axial damage value is higher than the radial damage value before the peak strength; whereas the radial damage value is higher than

the axial damage value after the peak strength. Furthermore, in the early cycles, the evolving rate of the radial damage is lower than that of the axial damage, but in the later cycles, the evolving rate of the radial damage is significantly higher than that of the axial damage, which indicates that the evolution of the mechanical parameters of sandstone specimen results mainly from the radial deformation damage.

It should be noted that the confining pressure has also a great effect on the axial and radial damage evolution of sandstone specimen. With the increase of cycle number, the axial and radial damage value of sandstone specimens all first increase slightly before the peak strength and then increase dramatically after the peak strength. From Fig. 25(a), we can see that the sandstone specimen with higher confining pressure has smaller damage value, which indicates that the confining pressure can reduce the extent of axial damage to rock. From Fig. 25(b), it can be seen that the evolving rate of the radial damage under lower confining pressure is significantly higher than that under higher confining pressure.

6 CONCLUSIONS

This paper explores the mechanical damage characteristics of sandstone using a series of triaxial cyclic experiments and X-ray micro-CT observations. Based on the experimental results, the following conclusions can be drawn:

(1) At lower confining pressures, the triaxial strength and elastic modulus of sandstone specimen under cyclic loading are all higher

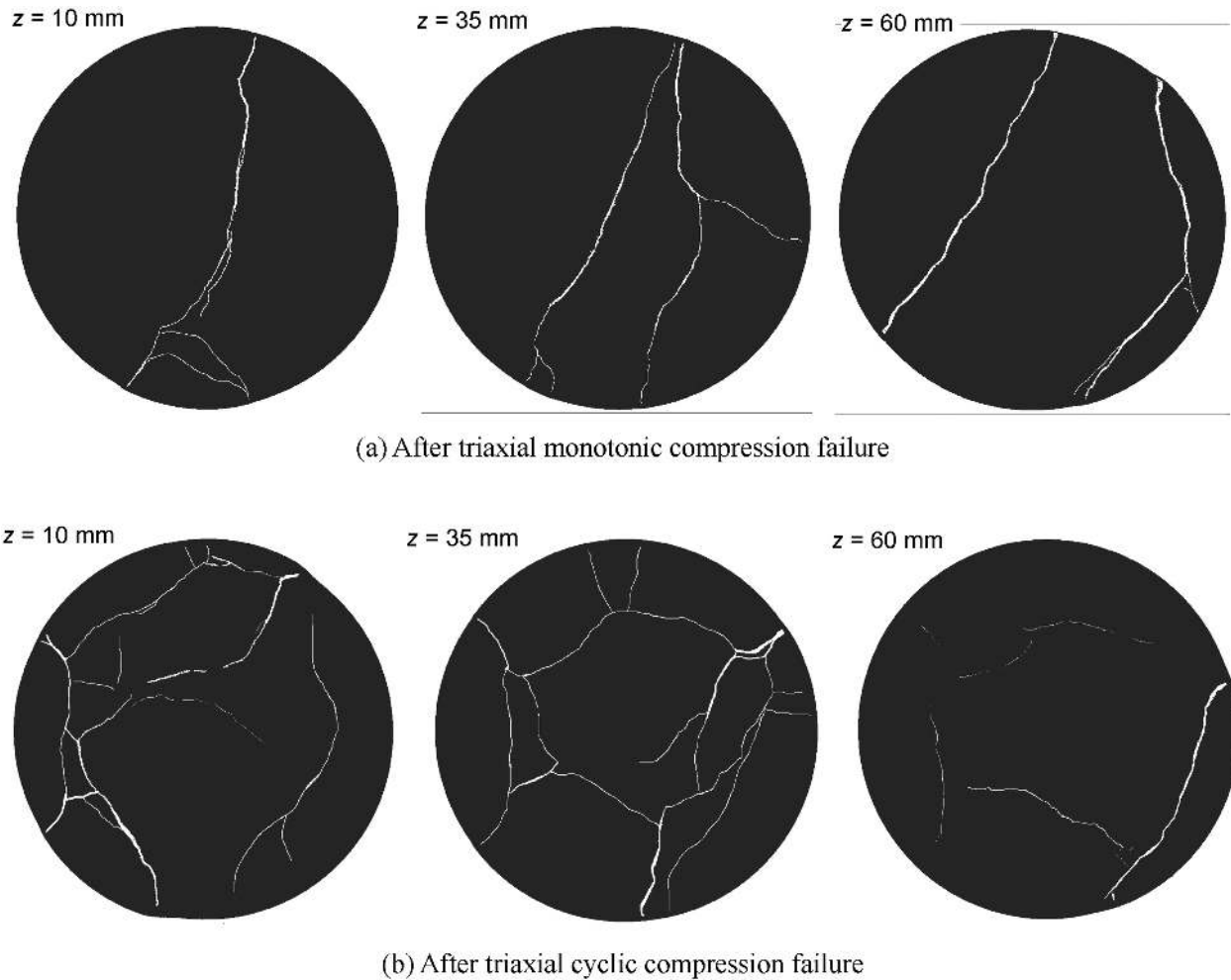


Figure 21. Typical binarized pictures of horizontal cross-sections of sandstone specimens after triaxial monotonic and cyclic compression failure ($\sigma_3 = 5$ MPa).

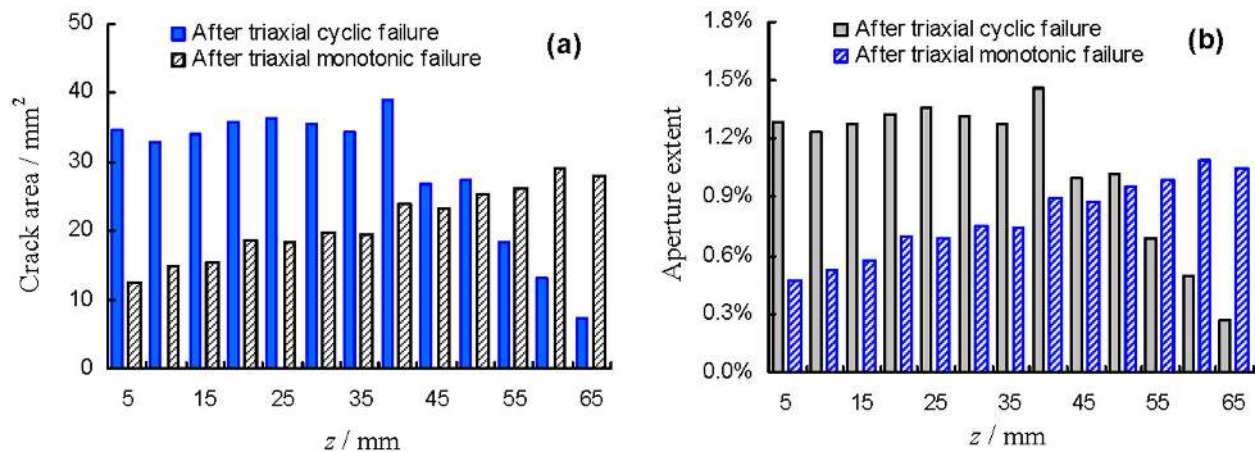


Figure 22. Evolution of crack area and aperture extent along different heights (z) of sandstone specimens after triaxial monotonic and cyclic compression failure ($\sigma_3 = 5$ MPa).

than those under monotonic loading. However, after confining pressure is increased to 20 MPa, the triaxial strength and elastic modulus of sandstone under cyclic loading are approximately equal to those under monotonic loading. The evolution of Young's modulus and Poisson's ratio of sandstone specimen with cycle number can be characterized as having four stages: (i) Stage I (material strengthen-

ing): the elastic modulus increases obviously, whereas the Poisson's ratio firstly decreases and then increases slightly; (ii) Stage II (material degradation): significant increase in Poisson's ratio and decrease in the elastic modulus are observed; (iii) Stage III (material failure): the elastic modulus of sandstone specimens decreases and the Poisson's ratio increases and (iv) Stage IV (structure slippage): there is

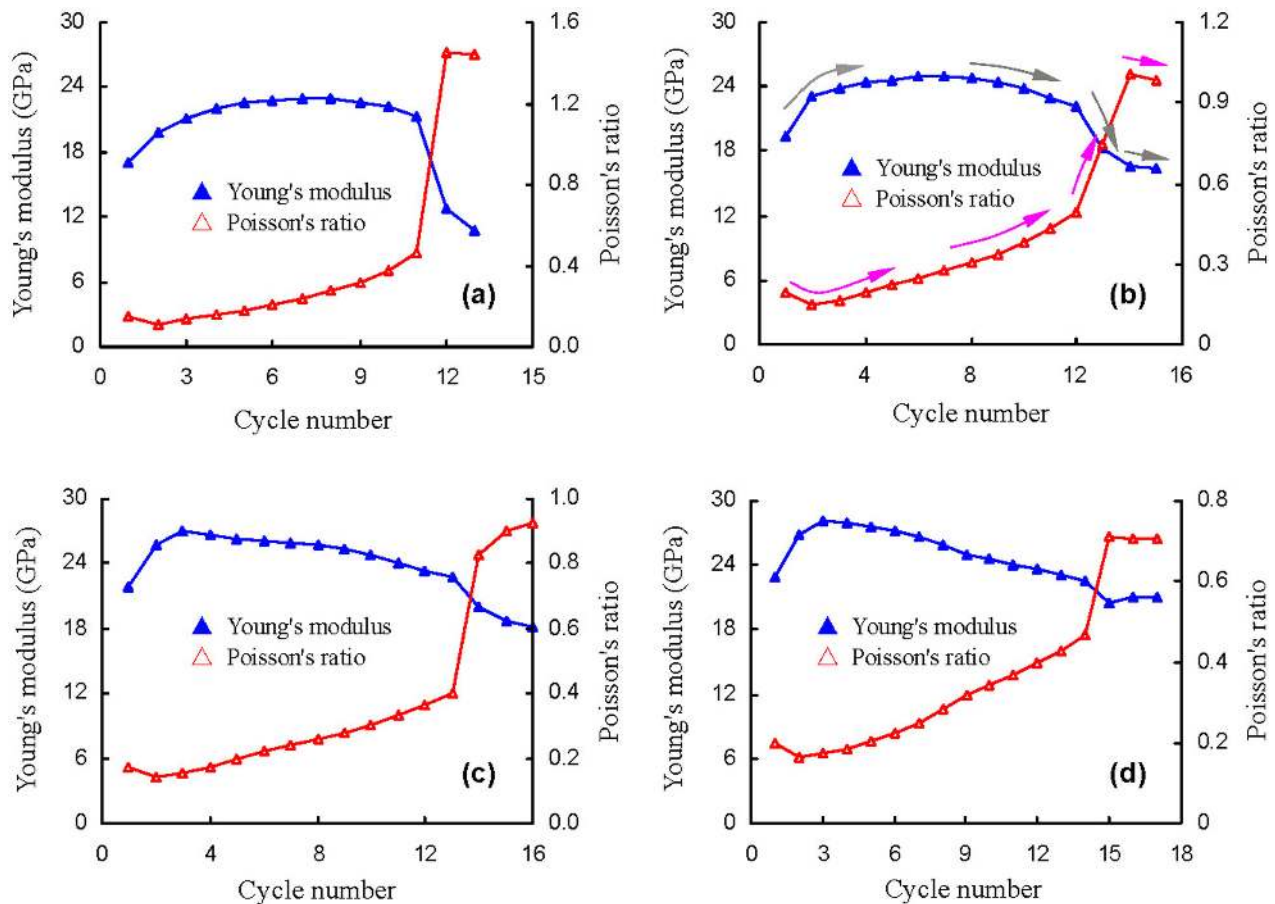


Figure 23. Evolution of elastic modulus and Poisson's ratio of sandstone specimens with the increase of cycle number. The arrows show the evolution direction of elastic modulus and Poisson's ratio. (a) $\sigma_3 = 5$ MPa; (b) $\sigma_3 = 10$ MPa; (c) $\sigma_3 = 20$ MPa and (d) $\sigma_3 = 30$ MPa.

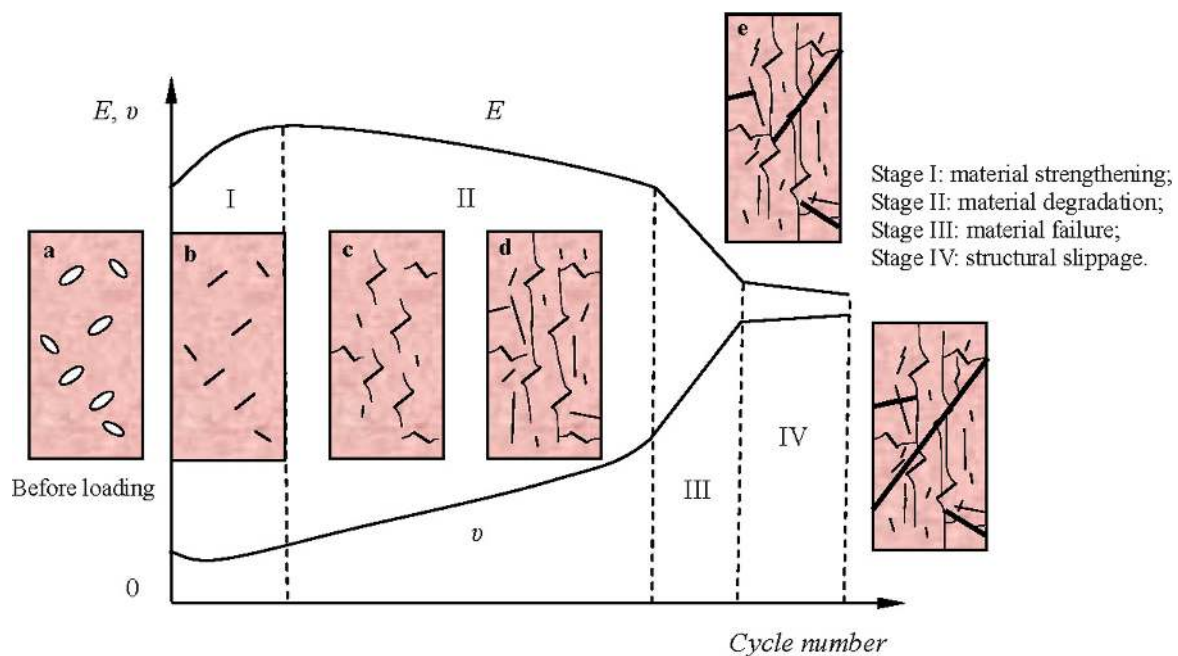


Figure 24. A sketch on four stages characterizing the evolution of elastic modulus and Poisson's ratio of sandstone specimens with the increase of cycle number under confining pressure.

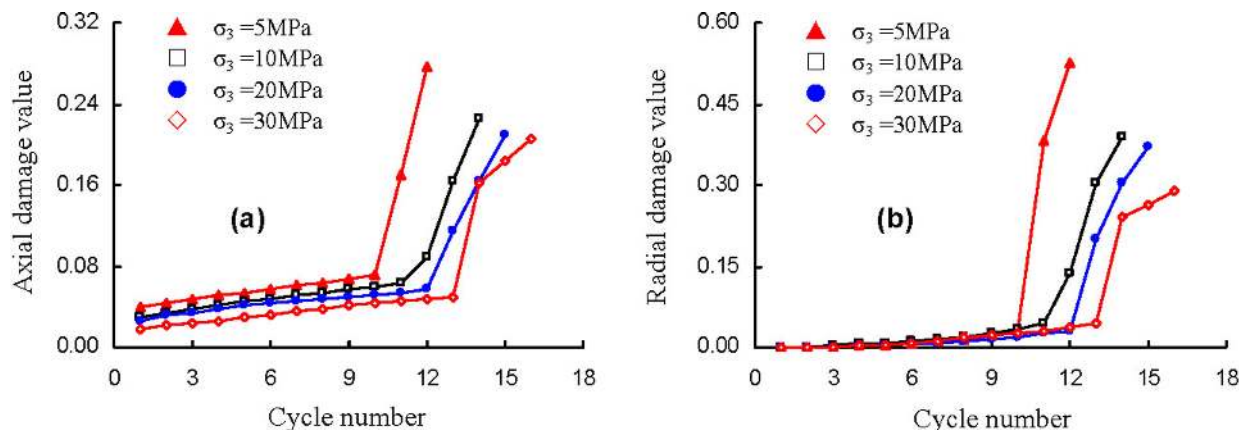


Figure 25. Influence of confining pressure on axial and radial damage evolution of sandstone. (a) Relation between axial damage value and cycle number; (b) relation between radial damage value and cycle number.

no obvious variance in both the elastic modulus and Poisson's ratio of sandstone specimens.

(2) With the increase of cycle number, the crack damage threshold of sandstone specimen firstly increases, and then significantly decreases, and finally remains constant. Furthermore, the above variance does not depend on the confining pressure. At the same cycle number, the sandstone specimen with higher confining pressure has a larger crack damage threshold, which indicates that the sandstone is more difficult to switch from compaction-dominated to dilatancy-dominated under higher confining pressure. The axial damage value of sandstone is higher than the radial damage value before the peak strength; whereas the radial damage value is higher than the axial damage value after the peak strength. Furthermore, in the early cycles, the evolving rate of the radial damage is lower than that of axial damage, but in the later cycles, the evolving rate of the radial damage is significantly higher than that of axial damage, which indicates that the evolution of mechanical parameters of sandstone specimens results mainly from radial deformation damage.

(3) After triaxial monotonic and cyclic compression failure ($\sigma_3 = 5$ MPa), the sandstone specimens were analysed using an X-ray micro-CT scanning system. Firstly, the surface X-ray CT scanning surface images of sandstone specimens were in good agreement with actual surface crack photographs, which demonstrates that X-ray micro-CT scanning can be used to explore internal damage to rock material. Based on the horizontal and vertical cross-sections of sandstone specimens, the internal damage in sandstone specimen after triaxial monotonic and cyclic compression failure was evaluated quantitatively by analysing the crack area and aperture extent for each horizontal cross-section. Generally, the system of crack planes under triaxial cyclic loading is much more complicated than that under triaxial monotonic loading. More axial and lateral tensile cracks in the specimens under cyclic loading were observed than under monotonic loading. The system of cracks is also in good agreement with the evolution of crack area and aperture extent with the height.

ACKNOWLEDGEMENTS

This research was supported by the National Basic Research 973 Program of China (Grant Nos 2014CB046905, 2013CB036003), the National Natural Science Foundation of China (Grant No. 41272344), the Program for New Century Excellent Talents in

University (Grant No. NCET-12-0961), the Team Project Funded by 2014 Jiangsu Innovation and Entrepreneurship Program, the Fundamental Research Funds for the Central Universities (Grant Nos 2014YC10 and 2014XT03), and Outstanding Innovation Team Project in China university of Mining and Technology (Grant No. 2014QN002). The first author obtained financial support from a 2014 Endeavour Research Fellowship in Australia, which was greatly appreciated. The authors would also like to express their sincere gratitude to the editor Eduard Petrovsky, and two anonymous reviewers for their valuable comments, which have greatly improved this paper.

REFERENCES

- Akesson, U., Hansson, J. & Stigh, J., 2004. Characterisation of microcracks in the Bohus granite, western Sweden, caused by uniaxial cyclic loading, *Eng. Geol.*, **72**, 131–142.
- Bagde, M.N. & Petros, V., 2005. The effect of machine behavior and mechanical properties of intact sandstone under static and dynamic uniaxial cyclic loading, *Rock Mech. Rock Eng.*, **38**(1), 59–67.
- Bieniawski, Z.T., 1971. Deformation behavior of fractured rock under multiaxial compression, in *Structure, Solid Mechanics and Engineering Design. Proc. Southampton 1969 Civil Eng. Materials Conference*, pp. 589–598, ed. Te'eni, M., Wiley-Interscience.
- Earslan, N. & Williams, D.J., 2012. Investigating the effect of cyclic loading on the indirect tensile strength of rocks, *Rock Mech. Rock Eng.*, **45**, 327–340.
- Fairhurst, C.E. & Hudson, J.A., 1999. Draft ISRM suggested method for the complete stress-strain curve for the intact rock in uniaxial compression, *Int. J. Rock Mech. Mining Sci.*, **36**(3), 279–289.
- Feng, X.T., Chen, S.L. & Zhou, H., 2004. Real-time computerized tomography (CT) experiments on sandstone damage evolution during triaxial compression with chemical corrosion, *Int. J. Rock Mech. Mining Sci.*, **41**(2), 181–192.
- Fuenkajorn, K. & Phueakphum, D., 2010. Effects of cyclic loading on mechanical properties of Maha Sarakham salt, *Eng. Geol.*, **112**, 43–52.
- Gatellier, N., Pellet, F. & Loret, B., 2002. Mechanical damage of an anisotropic porous rock in cyclic triaxial tests, *Int. J. Rock Mech. Mining Sci.*, **39**, 335–354.
- Gui, Y.L., Zhao, G.F. & Khalili, N., 2012. Experimental investigation of desiccation of clayey soils, in *Proceeding of the 22th Australasian Conference on the Mechanics of Structure and Materials (ASMSM22)*, December 11–14, Sydney, Australia.
- Hawkes, I. & Mellor, M., 1970. Uniaxial testing in rock mechanics laboratories, *Eng. Geol.*, **4**, 177–285.

- Heap, M.J. & Faulkner, D.R., 2008. Quantifying the evolution of static elastic properties as crystalline rock approaches failure, *Int. J. Rock Mech. Mining Sci.*, **45**, 564–573.
- Heap, M.J., Baud, P., Meredith, P.G., Bell, A.F. & Main, I.G., 2009a. Time-dependent brittle creep in Darley Dale sandstone, *J. geophys. Res.*, **114**, doi:10.1029/2008JB006212.
- Heap, M.J., Vinciguerra, S. & Meredith, P.G., 2009b. The evolution of elastic moduli with increasing crack damage during cyclic stressing of a basalt from Mt. Etna volcano, *Tectonophysics*, **47**, 153–160.
- Heap, M.J., Faulkner, D.R., Meredith, P.G. & Vinciguerra, S., 2010. Elastic moduli evolution and accompanying stress changes with increasing crack damage: implications for stress changes around fault zones and volcanoes during deformation, *Geophys. J. Int.*, **183**, 225–236.
- Jafari, M.K., Hosseini, K.A., Pellet, F., Boulon, M. & Buzzi, O., 2003. Evaluation of shear strength of rock joints subjected to cyclic loading, *Soil Dyn. Earthq. Eng.*, **23**, 619–630.
- Liu, E.L. & He, S.M., 2012. Effects of cyclic dynamic loading on the mechanical properties of intact rock samples under confining pressure conditions, *Eng. Geol.*, **125**, 81–91.
- Liu, E.L., He, S.M., Xue, X.H. & Xu, J., 2011. Dynamic properties of intact rock samples subjected to cyclic loading under confining pressure conditions, *Rock Mech. Rock Eng.*, **44**, 619–634.
- Liu, J.F., Xie, H.P., Hou, Z.M., Yang, C.H. & Chen, L., 2014. Damage evolution of rock salt under cyclic loading in uniaxial tests, *Acta Geotech.*, **9**, 153–160.
- Ma, L.J. et al., 2013. Experimental investigation of the mechanical properties of rock salt under triaxial cyclic loading, *Int. J. Rock Mech. Mining Sci.*, **62**, 34–41.
- Mogi, K., 1966. Some precise measurements of fracture strength of rocks under uniform compressive stress, *Rock Mech. Eng. Geol.*, **4**, 41–55.
- Rao, M.V.M.S. & Ramana, Y.V., 1992. A study of progressive failure of rock under cyclic loading by ultrasonic and AE monitoring techniques, *Rock Mech. Rock Eng.*, **25**(4), 237–251.
- Song, H.P., Zhang, H., Kang, Y.L., Huang, G.Y., Fu, D.H. & Qu, C.Y., 2013. Damage evolution study of sandstone by cyclic uniaxial test and digital image correlation, *Tectonophysics*, **608**, 1343–1348.
- Sufian, A. & Russell, A.R., 2013. Microstructural pore changes and energy dissipation in Gosford sandstone during pre-failure loading using X-ray CT, *Int. J. Rock Mech. Mining Sci.*, **57**, 119–131.
- Trippetta, F., Collettini, C., Meredith, P.G. & Vinciguerra, S., 2013. Evolution of the elastic moduli of seismogenic Triassic Evaporites subjected to cyclic stressing, *Tectonophysics*, **592**, 67–79.
- Wang, Z.C., Li, S.C., Qiao, L.P. & Zhao, J.G., 2013. Fatigue behavior of granite subjected to cyclic loading under triaxial compression condition, *Rock Mech. Rock Eng.*, **46**, 1603–1615.
- Wong, T.F., David, C. & Zhu, W., 1997. The transition from brittle faulting to cataclastic flow in porous sandstones, *Mech. Deformat. J. Geophys. Res.*, **102**(B2), 3009–3025.
- Xiao, J.Q., Ding, D.X., Jiang, F.L. & Xu, G., 2010. Fatigue damage variable and evolution of rock subjected to cyclic loading, *Int. J. Rock Mech. Mining Sci.*, **47**, 461–468.
- Xu, J., Tang, X.J., Li, S.C., Tao, Y.Q. & Jiang, Y.D., 2009. Space-time evolution rules study on acoustic emission location in rock under cyclic loading, *Front. Archit. Civ. Eng. China*, **3**(4), 422–427.
- Xu, T., Tang, C.A., Zhao, J., Li, L.C. & Heap, M.J., 2012. Modelling the time-dependent rheological behavior of heterogeneous brittle rocks, *Geophys. J. Int.*, **189**(3), 1781–1796.
- Yang, S.Q., Jiang, Y.Z., Xu, W.Y. & Chen, X.Q., 2008. Experimental investigation on strength and failure behavior of pre-cracked marble under conventional triaxial compression, *Int. J. Solids Struct.*, **45**, 4796–4819.
- Yang, S.Q., Jing, H.W., Li, Y.S. & Han, L.J., 2011. Experimental investigation on mechanical behavior of coarse marble under six different loading paths, *Exp. Mech.*, **51**, 315–334.
- Yang, S.Q., Jing, H.W. & Wang, S.Y., 2012. Experimental investigation on the strength, deformability, failure behavior and acoustic emission locations of red sandstone under triaxial compression, *Rock Mech. Rock Eng.*, **45**, 583–606.
- Yang, S.Q. & Jing, H.W., 2013. Evaluation on strength and deformation behavior of red sandstone under simple and complex loading paths, *Eng. Geol.*, **164**, 1–17.
- Zhao, G.F., Russell, A.R., Zhao, X.B. & Khalili, N., 2014. Strain rate dependency of uniaxial tensile strength in Gosford sandstone by the Distinct Lattice Spring Model with X-ray micro CT, *Int. J. Solids Struct.*, **51**, 1587–1600.
- Zhu, W.C., Li, Z.H., Zhu, L. & Tang, C.A., 2010. Numerical simulation on rockburst of underground opening triggered by dynamic disturbance, *Tunnell. Underground Space Technol.*, **25**(5), 587–599.